

Abstract

We have retrieved the wavelength-dependent imaginary parts of the complex refractive index for five different Saharan dust aerosol particles of variable mineralogical composition at wavelengths between 305 and 955 nm. The dust particles were generated by re-dispersing soil samples into a laboratory aerosol chamber, typically yielding particle sizes with mean diameters ranging from 0.3 to 0.4 μm and maximum diameters from 2 to 4 μm . The extinction and absorption coefficients as well as the number size distribution of the dust particles were simultaneously measured by various established techniques. An inversion scheme based on a spheroidal dust model was employed to deduce the refractive indices. The retrieved imaginary parts of the complex refractive index were in the range from 0.003 to 0.005, 0.005 to 0.011, and 0.016 to 0.050 at the wavelengths 955, 505, and 305 nm. The hematite content of the dust particles was determined by electron-microscopical single particle analysis. Hematite volume fractions in the range from 1.1 to 2.7 % were found for the different dusts, a range typical for atmospheric mineral dust. We have performed a sensitivity study to assess how accurately the retrieved imaginary refractive indices could be reproduced by calculations with mixing rule approximations using the experimentally determined hematite contents as input.

1 Introduction

This contribution builds on our previous aerosol chamber study on the optical properties and mineralogical composition of different Saharan mineral dust samples (Linke et al., 2006). In the recent work, we have determined wavelength-dependent mass specific extinction, scattering, and absorption cross sections in the UV/VIS spectral region for airborne Saharan dust samples from different geographic locations and have related the deduced single scattering albedos to the iron oxide content of the samples. Such optical data are needed for a better assessment of the radiative impact of mineral dust due to the absorption and scattering of solar radiation (Sokolik and Toon, 1999).

Complex refractive indices of Saharan dust samples

R. Wagner et al.

Title Page

Abstract

Introduction

Conclusions

References

Tables

Figures



Back

Close

Full Screen / Esc

Printer-friendly Version

Interactive Discussion



The focus on iron oxides like hematite and goethite is related to their large absorption potential at visible and near UV wavelengths (Alfaro et al., 2004; Balkanski et al., 2007; Kandler et al., 2009; Lafon et al., 2004, 2006; Sokolik and Toon, 1999).

For the analysis of our present aerosol chamber experiments on the optical properties of re-suspended mineral dust samples, we have extended our data evaluation procedure in order to deduce the complex refractive indices of the dust aerosol particles from our optical measurements. The most recent effort to derive these basic input parameters for the calculation of the single scattering properties of dust aerosols was in the context of the Saharan Mineral Dust Experiments (SAMUM-1 and SAMUM-2) (Müller et al., 2010, 2011). Whereas the SAMUM-1 experiment took place in a source region of mineral dust in southern Morocco, the dust aerosol probed during SAMUM-2 was transported over long distances to the Cape Verde Islands. For a particular measurement day of SAMUM-1, Müller et al. (2010) have compared different techniques to derive the complex refractive indices of the observed dust plume. Firstly, a spheroidal dust model was used to deduce the complex refractive indices from Sun photometer observations with AERONET (Aerosol Robotic Network) (Dubovik et al., 2002b, 2006). Secondly, the results from airborne in situ measurements of the particle size distributions and the aerosol absorption coefficients by a three-wavelength Particle Soot Absorption Photometer (PSAP) were introduced into a Mie theory based data analysis scheme to infer the optical constants of the dust aerosol (Petzold et al., 2009). Thirdly, the imaginary part of the complex refractive index was obtained from another inversion scheme based on Mie scattering calculations using ground-based recordings of the particle number size distributions and the aerosol absorption coefficients by the Spectral Optical Absorption Photometer (SOAP) in the wavelength range from 300 to 800 nm as input data (Müller et al., 2009). Finally, the chemical composition of 12900 particles was investigated by electron microscopic single particle analysis (for the methods, refer to Kandler et al., 2009). The identified relative volume abundance of minerals was then simplified to a five-component mineralogical model and the aerosol complex refractive index of the particles was calculated by applying a volume mixing

Complex refractive indices of Saharan dust samples

R. Wagner et al.

Title Page

Abstract

Introduction

Conclusions

References

Tables

Figures

◀

▶

◀

▶

Back

Close

Full Screen / Esc

Printer-friendly Version

Interactive Discussion



rule using tabulated refractive indices of the model substances (Kandler et al., 2009 and references therein).

In Fig. 5 of Müller et al. (2010), the results for the real and imaginary part of the complex refractive index derived from the different techniques are compared. Although partly showing a reasonable agreement, as e.g. the spectra of the imaginary part derived from AERONET, PSAP, and SOAP, there still remain striking differences such as the entirely different wavelength dependence of the spectrum of the imaginary part retrieved from the single particle mineralogical analysis. Müller et al. (2010) have speculated that this might be due to the fact that the latter technique is unable to resolve potential amounts of soot and therefore only represents the pure dust contribution whereas the other measurements are sensitive to the total particle mixture. After applying a soot correction to the SOAP recordings (Müller et al., 2009), these data indeed show better agreement with the results from the mineralogical single particle analysis but are also associated with large uncertainty bars. Notwithstanding these recent advances from field measurements, we still consider it an urgent need to provide additional reliable data sets of complex refractive indices for dust aerosols of varying mineralogical composition, as also recently emphasised by Otto et al. (2009). Specifically addressing the absorption potential of mineral dust, we have selected for our present study dust samples with variable iron oxide content. Thereby, we want to better assess the variability of the spectrum of the imaginary part of the complex refractive index for hematite and/or goethite contents that are typical of desert dust aerosol particles. The well-characterised and controlled conditions of our laboratory experiments will help to minimise the uncertainties that are associated with the retrieved data sets.

As a guide for the reader, we briefly summarise our basic experimental approach. Five different Saharan dust aerosol particles were generated and added to a laboratory aerosol chamber via one or two impaction stages of a cyclone system, yielding number size distributions predominantly in the sub-micron particle diameter range. The wavelength-resolved aerosol extinction and absorption coefficients were independently measured in the regime from 230–1000 nm and 305–955 nm, respectively. An

Complex refractive indices of Saharan dust samples

R. Wagner et al.

Title Page

Abstract

Introduction

Conclusions

References

Tables

Figures

◀

▶

◀

▶

Back

Close

Full Screen / Esc

Printer-friendly Version

Interactive Discussion



2 Experimental

2.1 Set-up of the aerosol chamber experiments, aerosol generation and characterisation

The set-up of the aerosol chamber experiments, as schematically shown in Fig. 1, is only slightly modified compared to our preceding work (Linke et al., 2006). The experiments were conducted in the 3.7 m³ sized NAUA chamber, a stainless steel aerosol vessel that is part of the AIDA (Aerosol Interactions and Dynamics in the Atmosphere) facility of the Karlsruhe Institute of Technology. All experiments took place at ambient temperature (typically 296 K) and pressure. Since the employed aerosol and optical instruments sampled ex situ from the chamber volume, a constant flow of particle-free synthetic air of about 2 m³ h⁻¹ was added to the vessel to balance for the sampling flows and to maintain ambient pressure conditions, thereby ensuring a well-defined dilution rate of the aerosol during an experiment. A mixing fan was continuously operating throughout the experiments for achieving homogeneous conditions in terms of temperature and aerosol particle number concentration inside the aerosol vessel. In the preparation of each experiment, the chamber was evacuated with a vacuum pump to a final pressure of about 0.5 hPa, followed by a series of flushing cycles with particle-free synthetic air to reduce the background level of aerosol particles. The background particle number concentration was usually less than 2 cm⁻³.

The employed Saharan soil samples (see Sect. 3.1) were sieved to grain size fractions of less than 20 µm, 20 to 75 µm, and greater than 75 µm. For our experiments, we have used the 20–75 µm size fraction and have disregarded the other fractions. Mineral dust aerosol particles were then generated and added to the NAUA chamber by dispersing the 20–75 µm sieved fraction of the dry dust samples in a rotating brush disperser (Palas, RGB 1000), de-agglomerating the finest particles in an aerosol dispersion nozzle, and removing larger particles by one or two stages of a five-stage series cyclone system developed at Southern Research Institute (Birmingham, Alabama). Both the rotating brush disperser and the dispersion nozzle were operated with dry and

Complex refractive indices of Saharan dust samples

R. Wagner et al.

Title Page

Abstract

Introduction

Conclusions

References

Tables

Figures

◀

▶

◀

▶

Back

Close

Full Screen / Esc

Printer-friendly Version

Interactive Discussion



particle-free synthetic air. The dispersion pressure of the nozzle was 1.5 bar. The initial particle number concentrations, as measured with a condensation particle counter (CPC3022A, TSI), were in the range from 860 to 6500 cm⁻³. After aerosol injection, the NAUA chamber acted as a reservoir for the sampling instruments. During each experiment with a given dust sample, three to four synchronised measurements of the number size distribution as well as the extinction and absorption spectrum were conducted at a time interval of about 20 min in order to be able to average the results for the retrieved refractive indices from multiple measurements. No significant and systematic change in the optical properties of the dust particles could be detected on the time scale of the experiments (Linke et al., 2006). For all dust samples, experiments with two impaction stages of the cyclone system were conducted, yielding a cut-off $d_{(50)}$ of 1.2 μm (aerodynamic diameter). This was done to minimise particle losses by sedimentation in the horizontal sampling lines and in the long horizontal flow tube of the long-path extinction spectrometer LOPES (see Sect. 2.2). The systematic error in the deduced extinction coefficients was estimated to be less than 5 % (Linke et al., 2006). For two dust probes (Burkina Faso and SAMUM B3, see Sect. 3.1), additional experiments with only one impaction stage of the cyclone system were performed, yielding $d_{(50)}$ of 1.5–1.7 μm . Thereby, a significant volume fraction of the dust loading was in a size range above the threshold that contributed to extinction and absorption in the two-stage impaction experiments. Figure 2 exemplarily shows the measured number and volume size distribution of the re-dispersed SAMUM B3 dust sample for experiments with one and two impaction stages to underline the different cut-off $d_{(50)}$ diameters between both procedures. When using two stages of the impaction system, particles with $d_v < 1 \mu\text{m}$ contribute to 91 % of the total dust volume concentration whereas with one impaction stage, this fraction is only 47 %. Accepting a higher uncertainty due to potential sedimentation losses, these experiments might therefore shed some light on the size dependence of the deduced complex refractive indices.

The number size distribution of the dust particles was measured with a Scanning Mobility Particle Sizer (SMPS, TSI, mobility diameter range from 0.014 to 0.82 μm) and

Complex refractive indices of Saharan dust samples

R. Wagner et al.

Title Page

Abstract

Introduction

Conclusions

References

Tables

Figures

◀

▶

◀

▶

Back

Close

Full Screen / Esc

Printer-friendly Version

Interactive Discussion



an Aerodynamic Particle Sizer (APS, TSI, aerodynamic diameter range from 0.523 to 19.81 μm). The mobility equivalent diameter d_m from the SMPS measurement is related to the volume equivalent sphere diameter d_v of the non-spherical dust particles by $d_v = d_m/\chi$, with χ denoting the dynamic shape factor (Hinds, 1999). From the aerodynamic diameter d_{ae} measured by the APS instrument, d_v is calculated using χ and the particle density ρ_p according to:

$$d_v = \sqrt{\frac{\chi}{\rho_p}} d_{ae}. \quad (1)$$

The APS instrument detects the decreasing tail of the number size distribution towards large particle diameters which significantly contributes to the total volume concentration of the dust loading and thus to its absorption spectrum. In contrast, the mean diameter (arithmetic average) of the number size distribution of the various dust particles falls into the size regime of the SMPS measurement and is between 0.27 and 0.43 μm (Table 1). To combine the SMPS and APS measurements, the particle density ρ_p was set to 2.6 g cm^{-3} , as estimated from the mineralogical composition of the dust samples (Sect. 3) using tabulated densities for the pure minerals (Kandler et al., 2009). χ was individually adjusted for each dust type to match the SMPS and APS recordings in their overlapping size regime, yielding values between 1.17 and 1.35. Similar results for χ were recently obtained by Schladitz et al. (2009). Note that any uncertainties in χ and ρ_p have a huge impact on the accuracy of the derived imaginary part of the complex refractive index of the dust samples. The error in d_v calculated by Eq. (1) is propagated to the third power into the uncertainty of the volume concentration of the dust particles. Since light absorption by the dust particles is governed by their volume concentration, this error is directly transferred to the retrieved imaginary part (absorption index) of the complex refractive index (Bohren and Huffman, 1983). For this reason, as already indicated in the introduction and elaborated in more detail in Sect. 4.4, we have optimised the measured number size distributions of the dust particles with the help of their simultaneously recorded extinction spectra. In addition to the SAMUM B3

Complex refractive indices of Saharan dust samples

R. Wagner et al.

Title Page

Abstract

Introduction

Conclusions

References

Tables

Figures

◀

▶

◀

▶

Back

Close

Full Screen / Esc

Printer-friendly Version

Interactive Discussion



example shown in Fig. 2, further number size distributions for all dust types are shown in Sect. 4.4. Table 1 summarises the initial number concentrations as well as mean and effective diameters (Hansen and Travis, 1974) for all experiments with the different dust types. Note that two identical experiment series (i.e. employing the same number of impaction stages) were conducted with the Cairo 2 and SAMUM B2 soil samples.

2.2 Optical instrumentation

UV-VIS extinction coefficients of the dust particles were measured with a flow tube extinction spectrometer (LOPES, Long-Path Extinction Spectrometer) (Linke et al., 2006; Schnaiter et al., 2005; Wagner et al., 2009). The horizontally mounted stainless steel flow tube of 3 m length is equipped with a retro reflector for optical path folding to obtain an overall optical path length of 6 m. The extinction spectra were recorded from 230 to 1000 nm with a spectral resolution of 2.5 nm, using a deuterium/halogen lamp combination (Mikropack, model DH2000-FHS-DUV) as the light source. The light is coupled in and out of the flow tubes by specially designed two-fibre optical systems in combination with a 90° off-axis parabola mirror (Schnaiter et al., 2005). The transmitted light is analysed by a 2-channel UV-VIS diode array spectrometer (tec5, MCS UV-NIR) with 15 bit resolution. Taking all systematic errors into account, the measurement yields the accuracy in terms of the extinction coefficients of 40 Mm⁻¹ (Schnaiter et al., 2005; Wagner et al., 2009).

The absorption coefficients, σ_{abs} , of the dust particles were deduced from measurements with the Spectral Optical Absorption Spectrometer SOAP that has already successfully been applied during the SAMUM-1 and SAMUM-2 field experiments (Müller et al., 2009, 2011). A description of the SOAP and a characterisation with the focus on absorption by mineral dust can be found in Müller et al. (2011). A few main features of the SOAP are given in the following. The dust particles are deposited onto a fibre filter (Pallflex E70/2075W) and a sample spot is illuminated by light of a deuterium/halogen lamp combination (Avantes, model AvaLight-DHS-DUV). The transmitted and reflected light is detected with two optical spectrometers (Control Development

Complex refractive indices of Saharan dust samples

R. Wagner et al.

Title Page

Abstract

Introduction

Conclusions

References

Tables

Figures

◀

▶

◀

▶

Back

Close

Full Screen / Esc

Printer-friendly Version

Interactive Discussion



Inc., CDI2DMPP-UV-VIS) at wavelengths between 200 to 960 nm with an optical resolution of 25 nm. The pixel resolution of the spectrometers is $1.5 \text{ nm pixel}^{-1}$ and raw data are smoothed to yield a resolution of 10 nm. Signals at wavelengths smaller 300 nm are too noisy and were not used. Data are given between 305 and 955 nm in steps of 10 nm. With an inversion scheme based on radiative transfer calculations of particle laden filters, particle absorption coefficients are calculated. A well known issue of filter based absorption measurements is the cross sensitivity to particle scattering. The effect of particle scattering is compensated for by measuring both the transmitted and reflected intensities. The uncertainties of SOAP are given by $\Delta\sigma_{\text{abs}} = \pm (0.15 \sigma_{\text{abs}} + 0.02 \sigma_{\text{sca}})$ (Müller et al., 2011). This implies that the uncertainty is a function of the single scattering albedo.

The absorption coefficients measured by SOAP were used in our inversion scheme to deduce the imaginary parts of the complex refractive index because they are continuously available over the entire wavelength range from 305 to 955 nm. The onset of dust absorption due to potential contributions of iron oxides can thus be accurately localised. Since we have used a photo acoustic system in our previous work to measure dust absorption (Linke et al., 2006), we want to briefly note that in the present study absorption measurements were additionally performed with a novel four wavelength photo acoustic spectrometer ($4\lambda - \text{PAS}$) that was developed at the University of Szeged, Hungary (Ajtai et al., 2010). Photo acoustic signals are obtained at the fundamental ($\lambda = 1064 \text{ nm}$), the doubled ($\lambda = 532 \text{ nm}$), the tripled ($\lambda = 355 \text{ nm}$), and the quadrupled ($\lambda = 266 \text{ nm}$) emission of a Nd:YAG laser. We will show a comparison of the records from the two instruments in Sect. 5.1.

2.3 Single particle analyses by electron microscopy

Dust aerosol particles were collected with a miniature cascade impactor on carbon adhesive and on Nickel grids with formvar/carbon foil (Plano, Wetzlar Germany). The samples were analysed by scanning electron microscopy (SEM) and transmission electron microscopy (TEM). Single particle analysis was performed with an FEI ESEM

Complex refractive indices of Saharan dust samples

R. Wagner et al.

Title Page

Abstract

Introduction

Conclusions

References

Tables

Figures

◀

▶

◀

▶

Back

Close

Full Screen / Esc

Printer-friendly Version

Interactive Discussion



Quanta 200 FEG equipped with an EDAX analysing system for single particle applications and a FEI TEM CM200. Both instruments were equipped with an energy-dispersive X-ray detector to assess the elemental composition of the single particles. Five components (quartz, an “average” silicate, hematite, calcite, and sulphate) were assumed to be representative of the aerosol composition. The relative contribution of these compounds was determined from the quantification of the tracer elements (Si, Si+Al, Fe, Ca, S, respectively) for each single particle. For more details on the technique, refer to Kandler et al. (2009).

The size of the particles used for their classification into intervals was calculated as

$$d_{\theta} = \sqrt{\pi^{-1}4B} \quad (2)$$

with B denoting the area covered by the particle. The shape of the particles was determined as the axis ratio, AR, of an equal area ellipse for each particle, calculated as

$$AR = \frac{\pi L^2}{4B} \quad (3)$$

with L denoting the longest projection of the particle outline.

3 Desert dust samples

3.1 Origin of the employed Saharan soil samples

Amongst the five dust samples listed in Table 1, the Cairo 2 sample has already been investigated in our previous study (Linke et al., 2006). This soil sample was collected from the Northern Sahara about 70 km northeast of Cairo city from a depth of 0.5 m and its colour is light yellow to light brown. Three further yellow brown coloured soil samples were collected during the SAMUM-1 field campaign in Morocco. The SAMUM B1 sample was collected in the Drâa valley 3 km west of M’Hamid (29°50.264’ N

Complex refractive indices of Saharan dust samples

R. Wagner et al.

Title Page

Abstract

Introduction

Conclusions

References

Tables

Figures

◀

▶

◀

▶

Back

Close

Full Screen / Esc

Printer-friendly Version

Interactive Discussion



5°45.686' W), the SAMUM B2 sample from a Hamada close to the Oued el Atach (29°50.974' N 6°0.905' W), and the SAMUM B3 sample in a dry river bed close to the border of the dry salt/silt plain of Lac Iriqui and to the sand dune fields (29°51.721' N 6°9.406' W). In contrast to these comparatively light-coloured soil samples, the fifth sample, Burkina Faso, has a much darker appearance and is coloured reddish brown. The Burkina Faso soil sample consists of wind-blown material and was collected in West Africa during the AMMA (African Monsoon Multidisciplinary Analysis) dust experiment near Dano (11°9.75' N 3°4.57' W) from the bank of an artificial lake which was bare of vegetation and not contaminated by sediments of the lake.

3.2 Bulk analyses of the chemical and mineralogical composition of the soil samples

The elemental composition of each soil sample was determined for the 20–75 µm size fraction by X-ray Fluorescence Analysis (XRF, Bruker AXS, SRS 303AS). Prior to the analysis, each soil sample was ignited at 1000 °C for 1 h and its loss on ignition was determined. A sample mass of 200 mg was used for the analysis. Table 2 summarises the weight percentages of oxides that were calculated from the measured elements. The total iron content (expressed by the method as Fe₂O₃) varies between 4.0 and 8.4 weight percent (wt%) and, as expected, is highest for the reddish brown coloured Burkina Faso soil sample. For assessing the absorption potential of the soil samples, however, the total iron content must be divided into two classes. Structural iron is incorporated into the crystal structure of silicates and alumino-silicates and does not considerably influence the optical properties at visible wavelengths (Karickhoff and Bailey, 1973; Lafon et al., 2004). Only Fe(III) in the form of oxides and hydroxides (Fe₂O₃, hematite; FeOOH, goethite), i.e. so-called free iron, controls absorption of light in soil samples (Lafon et al., 2004). The free-to-total iron ratio in natural soil samples can be highly variable. Lafon et al. (2006), for example, have measured percentages of free-to-total iron from 43–75 % for various dust samples. Based on an average compiled

Complex refractive indices of Saharan dust samples

R. Wagner et al.

Title Page

Abstract

Introduction

Conclusions

References

Tables

Figures

◀

▶

◀

▶

Back

Close

Full Screen / Esc

Printer-friendly Version

Interactive Discussion



from the literature, Kandler et al. (2009) have assumed that only 20 % of the total iron content is hematite. It is therefore necessary to obtain independent information on the mineralogical composition of the soil samples by X-ray Diffraction Analysis (XRD).

The mineralogy of the 20–75 μm sieved fraction of the Burkina Faso, SAMUM B1, B2, and B3 soil samples was identified and quantified by X-ray Diffraction using the method of reference intensity ratios (RIR) (Chung, 1974). The standard-less RIR method uses the intensities of the main reflections of the mineral phases to calculate the relative mineral abundances, relying on RIR values of the minerals that are provided by the ICDD database (ICDD, 2002). Note that only identified minerals are summed up to 100 %. Special care has to be taken to quantify clay minerals because they usually exhibit no or only weak reflections in randomly oriented powder samples due to their small particle size and their crystal structure (Moore and Reynolds, 1997). As described in Kandler et al. (2009), we have therefore additionally created textured samples to obtain a preferential horizontal orientation of the predominantly plate-like clay mineral particles. This induces an enhancement of their X-ray peak intensities, thereby facilitating mineral identification. To calculate the total weight fraction of clay minerals, we define a threshold size of 2 μm and assign all particles below this size to the clay fraction. The two size fractions <2 μm and >2 μm were separated by gravimetric methods and then independently weighed to evaluate the clay content (Kandler et al., 2009). In the final analysis step, a randomly oriented sample of the <2 μm clay fraction was prepared to quantify the clay minerals afore identified in the textured specimens.

Table 3 summarises the results from the XRD bulk analyses of the four soil samples. The three SAMUM soil samples have a similar composition, with a quartz content of 31–49 wt % and 29–37 wt % fractions of the feldspars albite and microcline. The lower quartz content of the SAMUM B2 sample is compensated by a higher amount of the clay minerals chlorite and kaolinite. In each sample, the iron oxide content (hematite and/or goethite) does not exceed 1 wt %. In contrast, the Burkina Faso sample shows a very high content of iron oxides (15 wt %) with a hematite to goethite ratio of 4:1. The other dominant mineral phases are quartz (52 wt %), muscovite (8 wt %), as well

Complex refractive indices of Saharan dust samples

R. Wagner et al.

Title Page

Abstract

Introduction

Conclusions

References

Tables

Figures

◀

▶

◀

▶

Back

Close

Full Screen / Esc

Printer-friendly Version

Interactive Discussion



as the clay minerals kaolinite and illite (19 and 6 wt%, respectively). Compared to the total iron contents determined by the XRF analyses which only vary by a factor of about two between the Burkina Faso and the three SAMUM soil samples, the XRD bulk analyses suggest that the absorption potential of the re-dispersed Burkina Faso soil sample should be at least one order of magnitude larger than that of the other soil probes. In the next section, we will investigate whether this large variation in the iron oxide content of the bulk soil samples is also evident in the actual aerosol composition of the re-dispersed dust particles, as inferred from electron-microscopic single particle analysis.

3.3 Single-particle analyses of the chemical and mineralogical composition of the airborne, re-dispersed dust particles

The automated analysis by scanning electron microscopy yields a backscatter electron image and an average elemental composition for each single particle. According to this elemental composition, particles are classified into major compositional groups following a set of criteria used successfully for mineral dust (e.g. Kandler et al., 2007, 2009). Figure 3 shows the size-resolved composition of the Burkina Faso and the SAMUM B1, B2, and B3 samples. In contrast to the bulk samples that were dominated by quartz (silicon dioxide), all aerosol samples are dominated by the silicate particle group (clay minerals and/or feldspars, indicated by the elements Si and Al, with minor contents of Na, Ca, K, and/or Fe). As expected from other investigations (e.g. Kandler et al., 2009), the obviously larger quartz particles from the parent soils were not present any more in the re-dispersed aerosol. A common feature for all samples is the increase in the abundance of iron-rich particles with decreasing particle size. In the Burkina Faso sample, this abundance of iron-rich particles is significantly higher than in the SAMUM samples, but the difference is much lower than the difference between the parent soil samples (Table 3). It can be concluded that – though iron seems to be associated rather with small particles in the aerosol – the largest amount of hematite and goethite was present in large grains removed by the re-dispersion of the soil samples. The

Complex refractive indices of Saharan dust samples

R. Wagner et al.

Title Page

Abstract

Introduction

Conclusions

References

Tables

Figures

◀

▶

◀

▶

Back

Close

Full Screen / Esc

Printer-friendly Version

Interactive Discussion



Complex refractive indices of Saharan dust samples

R. Wagner et al.

[Title Page](#)[Abstract](#)[Introduction](#)[Conclusions](#)[References](#)[Tables](#)[Figures](#)[⏪](#)[⏩](#)[◀](#)[▶](#)[Back](#)[Close](#)[Full Screen / Esc](#)[Printer-friendly Version](#)[Interactive Discussion](#)

total hematite volume contribution to the aerosol, as calculated by the five component mixing model, is 2.7 vol% for the Burkina Faso sample and only 1.1 to 1.6 vol% for the SAMUM samples (Table 4). As in Kandler et al. (2009), 20% of the total iron content were attributed to hematite. Another visible difference between the Burkina Faso sample and the SAMUM samples lies in the presence of calcium-rich particles, which are absent in the Burkina Faso sample, but contribute with up to 9.2 vol% to the SAMUM samples. This difference is in accordance with the parent topsoil composition of the source regions (Claquin et al., 1999). In Sect. 5.2, we employ the deduced aerosol composition from Table 4 as input to compute the imaginary parts of complex refractive index of the dust particles with various mixing rule approaches.

The particles were classified into compositional groups to enable the calculation of volume contributions; however, even though this complexity cannot currently be regarded by our model, it should not be concealed that each single particle can possess a unique composition and structure. Figure 4 shows a scatter plot of iron index versus silicon index. The element index is defined as the atomic ratio of the concentration of the element considered and the sum of the concentrations of the elements Na, Mg, Al, Si, P, S, Cl, K, Ca, Ti, Cr, Mn, and Fe. It becomes instantaneously visible that a) the average iron index of the silicate particles is larger in Burkina Faso (cluster around silicon index 0.45), and that b) there exists a group of small particles rich in iron (cluster at silicon index 0.1 and iron index 0.5), which is more abundant in the Burkina Faso than in the SAMUM B3 sample. Apart from these clusters, particles with variable compositions exist. For this reason, the five component mixing model described above was calculated on a single particle basis rather than based on the identified particle groups.

To illustrate the complex structure of even single particles, Fig. 5 shows an example from the Burkina Faso dust sample. The particle is composed of silicate (Si+Al) particles with small grains of nanometre-sized crystallites of iron oxides either as inclusions or on the surface, which have also been described for atmospheric aerosol (Lieke et al., 2011). These iron oxide nanocrystallites were determined to consist of

hematite by selected area diffraction (SAED) in the TEM. Lattice spacings measured in the SAED patterns did match with hematite, but neither with magnetite nor goethite. High resolution TEM images of those iron enriched locations on the particles revealed primary crystallite grains of five to some tens of nanometres size. Additional elemental mappings (not shown) revealed that iron-rich and also titanium-rich crystallites on and attached to particles are a common feature of the investigated dust, which was also reported for atmospheric desert aerosol (e.g. Scheuvens et al., 2011). The complexity of the internal particle structure must be kept in mind when comparatively simple mixing rule approaches are applied to compute the complex refractive index of the dust particles (Sect. 5.2).

The shape of the dust particles was assessed by means of an axis ratio of an equal-area ellipse for all analysed particles (Sect. 2.3). This information is important to cover the appropriate regime of particle aspect ratios in the computation of the optical cross sections whose methodology is described in the next section. In Fig. 6, the density distribution of the axis ratios (AR) is shown as normalised values per size interval as well as a parameterised curve (for parameterisation refer to Kandler et al., 2007). While there is no considerable difference between the SAMUM B1 and B3 samples (median AR for B1/B2/B3:1.85/1.93/1.78; particle number of B2 was not sufficient for parameterisation), the Burkina Faso sample shows slightly lower axis ratio values (median 1.69), i.e. less elongated particles. Overall, the AR values found in this laboratory experiment are slightly higher than those encountered in ambient dust aerosol, featuring median values of 1.6 to 1.7 west of Africa with similar parent soils (Kandler et al., 2007, 2009, 2011). This might be related to the aerosol generation mechanism because the re-dispersion of the soil samples including one or two impaction stages is, of course, just a surrogate for the natural particle production.

Complex refractive indices of Saharan dust samples

R. Wagner et al.

Title Page

Abstract

Introduction

Conclusions

References

Tables

Figures

◀

▶

◀

▶

Back

Close

Full Screen / Esc

Printer-friendly Version

Interactive Discussion



4 Inversion scheme

In this chapter, we explain the details of our inversion scheme to deduce the wavelength dependent imaginary part of the complex refractive index of the airborne dust particles from their optical spectra and their simultaneously recorded number size distributions. In Sect. 4.1, we describe the computation of a scattering database on a four-dimensional parameter space which serves as a look-up table in the retrieval procedure and thus limits the computational burden of our analysis. The database contains the extinction and absorption cross sections of randomly-oriented spheroidal particles as a function of their size parameter, aspect ratio, and the real and imaginary parts of the complex refractive index. Selected computational results on the shape dependency of the optical cross sections are summarised in Sect. 4.2. In Sect. 4.3, we outline our initial approach aiming at the retrieval of both the real and the imaginary part of the complex refractive index from the extinction and the absorption spectrum. Our modified approach where the extinction spectrum is used for optimising the measured number size distribution of the dust particles which then is used as input to derive the imaginary part of the complex refractive index from the absorption spectrum is described in Sect. 4.4.

4.1 Computational methods: a database of optical cross sections for randomly oriented spheroidal particles

As in similar computational studies on the optical properties of mineral dust, we have employed a spheroidal model to compute the shape dependent extinction and absorption cross sections of the irregularly shaped dust particles (Dubovik et al., 2006; Meng et al., 2010; Merikallio et al., 1997, 2011; Otto et al., 2009; Wiegner et al., 2009; Yang et al., 2007). A random orientation of the particles was assumed. The aspect ratio ε of a spheroid was defined as the ratio of its horizontal to rotational axis (Mishchenko and Travis, 1998). Both oblate ($\varepsilon > 1$) and prolate ($\varepsilon < 1$) particle shapes were considered in the calculations. Given the aspect ratio density distribution obtained from the

Complex refractive indices of Saharan dust samples

R. Wagner et al.

Title Page

Abstract

Introduction

Conclusions

References

Tables

Figures

◀

▶

◀

▶

Back

Close

Full Screen / Esc

Printer-friendly Version

Interactive Discussion



SEM single particle analyses (Fig. 6), a maximum asphericity of $\varepsilon = 4$ and $\varepsilon = 0.25$ was assumed for oblate and prolate particle shapes, respectively. Altogether, 29 logarithmically equidistant aspect ratios between 0.25 and 4 were considered. For each aspect ratio, the optical cross sections were computed for 88 logarithmically spaced equal-volume sphere size parameters x_v ($x = \pi d_v / \lambda$) between 0.02 and 50, 11 equidistantly spaced real parts of the complex refractive index between 1.3 and 1.7, and 15 logarithmically spaced values between 0.0001 and 0.1 for the imaginary part of the complex refractive index, summing up to 14 520 individual calculations. The optical cross sections for intermediate values of x_v and the complex refractive index are obtained by spline interpolation from the pre-computed data.

We have calculated the extinction and absorption cross sections of the spheroids with the extended precision FORTRAN T-matrix code for randomly oriented particles by Mishchenko and Travis (1998) up to size parameters where stable performance was guaranteed. For large deviations from the spherical shape, the T-matrix computations became non-convergent before the largest considered size parameter of $x_v = 50$ was reached. Beside ε , this convergence limit also depends on the magnitude of the real and imaginary part of the complex refractive index (Mishchenko and Travis, 1998). Above the convergence point of the T-matrix calculations, we have continued our computations with a ray-tracing model including diffraction of light incident on the particles' projected area (Macke et al., 1996). In the framework of the geometric optics approximation with the allowance for diffraction, the extinction efficiency Q_{ext} (extinction cross section, C_{ext} , divided through the average cross-sectional area of the particles) is equal to 2 and the value for the absorption efficiency, Q_{abs} , does not exceed unity. In reality, however, the limit $Q_{\text{ext}} = 2$ is only reached for size parameters well above our considered size range and absorption resonances might occur with $Q_{\text{abs}} > 1$ (Baran et al., 2001). The differences between the true extinction and absorption efficiencies Q_{ext} and Q_{abs} calculated with the T-matrix method and their counterparts calculated in the geometric optics approximation are called the edge contributions (Baran and Havemann, 1999; Fournier and Evans, 1991; Kokhanovsky and Zege, 1995; Yang et al., 2007).

Complex refractive indices of Saharan dust samples

R. Wagner et al.

[Title Page](#)[Abstract](#)[Introduction](#)[Conclusions](#)[References](#)[Tables](#)[Figures](#)[⏪](#)[⏩](#)[◀](#)[▶](#)[Back](#)[Close](#)[Full Screen / Esc](#)[Printer-friendly Version](#)[Interactive Discussion](#)

The edge contribution to the extinction efficiency for randomly oriented spheroids was calculated according to the approximations by Fournier and Evans (1991). Similar to Yang et al. (2007), the edge contribution to the absorption efficiency of a spheroid of diameter d_v was in the first step approximated to be equal to that of an equal-volume sphere. The latter quantity was calculated as the difference between the true absorption efficiency calculated with Mie theory and the geometric optics result.

Two examples of the applied edge corrections are displayed in Fig. 7. In the left panel, we show an example where the T-matrix computations were convergent over the complete range of size parameters (oblate spheroids with $\varepsilon = 2$, complex refractive index = $1.5 + 0.1 i$) in order to assess the accuracy of the edge correction. Whereas the pure geometric optics results for the extinction and absorption efficiencies reveal clear deviations from the T-matrix values for the reasons outlined in the preceding paragraph, the addition of the edge contribution leads to a very good agreement with the T-matrix result for size parameters larger than about 15. In the second example shown in the right panel, we have increased ε to 2.97. The convergence limit of the T-matrix computations is at about $x_v = 31$. For the extinction efficiency, an accurate extension of the truncated T-matrix results is obtained by including the edge contribution. The absorption efficiency at the threshold size parameter of $x_v = 31$, however, is slightly overestimated when adding the edge contribution of an equal-volume sphere to the geometric optics result (dashed blue line). A better extension of the Q_{abs} curve is obtained when equalling the edge contribution to that of an equal-volume spheroid of $\varepsilon = 2$ (dashed red line, obtained as difference from the true Q_{abs} calculated by the T-matrix method and the geometric optics result). In the second step, we have therefore computed the edge contribution to Q_{abs} for prolate and oblate spheroids with the largest asphericity for which stable T-matrix results could be obtained over the complete range of size parameters. These values were then used to improve the geometric optics results of Q_{abs} for spheroids of higher asphericity at size parameters where the T-matrix calculations did not converge.

Complex refractive indices of Saharan dust samples

R. Wagner et al.

Title Page

Abstract

Introduction

Conclusions

References

Tables

Figures

◀

▶

◀

▶

Back

Close

Full Screen / Esc

Printer-friendly Version

Interactive Discussion



4.2 Shape dependency of the computed extinction and absorption cross sections

In Fig. 8, we have compiled selected computational results from the database to underline the shape dependency of the optical cross sections of the randomly oriented spheroids. The left panel shows the extinction cross sections as a function of the particles' equal-volume sphere diameter at a wavelength of 500 nm for a complex refractive index of $1.5 + 0.014 i$. A set of curves for all considered aspect ratios is shown, with selected shapes highlighted by coloured lines. Up to a d_v of about $0.7 \mu\text{m}$, the spread of the individual traces is low. As evident from the insert, an increasing degree of particle asphericity leads to a slight decrease in the extinction cross sections. As an example, C_{ext} for $0.5 \mu\text{m}$ sized spheroids of aspect ratio $\varepsilon = 0.25$ (red line) is lowered by about 10% compared to spheres (green line). Larger deviations from the results for spheres in this size regime are only expected for particles with extreme aspect ratios, e.g. needle- and plate-like particles (Zakharova and Mishchenko, 2000).

Above $0.7 \mu\text{m}$, the results for the extinction cross sections of the various spheroidal particle shapes start to diverge because we enter the size range where extinction is governed by the interference structure, i.e. series of extinction minima and maxima caused by interference of incident and forward-scattered light (Bohren and Huffman, 1983). The interference structure can be better seen when plotting the extinction efficiencies as a function of d_v , as shown in the right panel of Fig. 8. For slightly aspherical spheroids (e.g. $\varepsilon = 1.64$, yellow line), the regular series of extinction minima and maxima observed for spheres (green line) is still conserved. A higher degree of asphericity, however, induces a strong distortion of these regular oscillations. Oblate spheroids of aspect ratio $\varepsilon = 4$ (brown line), for example, show a first extinction efficiency maximum at $d_v = 1.2 \mu\text{m}$ whereas for spheres this particle size corresponds to the first extinction minimum after having already surpassed the first extinction maximum at $d_v = 0.7 \mu\text{m}$. The extinction cross section (left panel) of $1.2 \mu\text{m}$ sized $\varepsilon = 4$ spheroids is thereby more than a factor of two higher than that of spheres. These pronounced shape dependent

Complex refractive indices of Saharan dust samples

R. Wagner et al.

[Title Page](#)[Abstract](#)[Introduction](#)[Conclusions](#)[References](#)[Tables](#)[Figures](#)[⏪](#)[⏩](#)[◀](#)[▶](#)[Back](#)[Close](#)[Full Screen / Esc](#)[Printer-friendly Version](#)[Interactive Discussion](#)

variations in C_{ext} will again be addressed in the discussion of our modified retrieval approach in Sect. 4.4 because, depending on the wavelength, a significant part of the dust particle number size distributions may extend into the size range that is dominated by the interference structure.

In addition to the spheroid computations, we have performed a single test calculation of C_{ext} and C_{abs} for an aggregate-like particle that might be a better representation for the habit of irregularly formed natural dust grains. The aggregate particle was modelled as two touching spheroids with individual aspect ratios of 1.07 and 1.20. The two spheroids have a volume ratio of 1.12 and an angle between their individual rotational axes of 45° . The optical cross sections of the aggregate particle in random orientation were computed with the discrete dipole approximation (DDA), using the DDSCAT 6.0 FORTRAN software package (Draine and Flatau, 1994). The trace for C_{ext} of the two touching ellipsoids, shown as blue line in the left panel, is up to a d_v of about $1.1 \mu\text{m}$ very similar to that of the most elongated spheroid ($\varepsilon = 0.25$, red line), a finding that will also again be discussed in Sect. 4.4.

The bottom panel of Fig. 8 displays the shape dependent absorption cross sections for the 29 considered spheroidal particle shapes as well as for the aggregate-like particle. For equal-volume sphere diameters up to about $1.5 \mu\text{m}$, the individual traces coincide, meaning that C_{abs} is proportional to the particle volume and does not show any variations with increasing asphericity as long as d_v is kept constant. For all dust experiments where two impaction stages were used during aerosol generation, almost the entire particle volume concentration is governed by particles of d_v less than $1.5 \mu\text{m}$ (Fig. 2). Hence, shape effects can be neglected when retrieving the imaginary part of the complex refractive index from the absorption spectra. Above $1.5 \mu\text{m}$, the individual traces for C_{abs} start to diverge slightly, with up to 10% higher values for the most aspherical spheroidal shapes compared to spheres at $d_v = 2.0$. This is an indication that C_{abs} becomes sensitive to the surface area of the particles (Bohren and Huffman, 1983). More elongated or flattened spheroids with $\varepsilon = 0.25$ or $\varepsilon = 4$ start to reveal slightly higher absorption cross sections compared to spheres or more compact

Complex refractive indices of Saharan dust samples

R. Wagner et al.

[Title Page](#)[Abstract](#)[Introduction](#)[Conclusions](#)[References](#)[Tables](#)[Figures](#)[⏪](#)[⏩](#)[◀](#)[▶](#)[Back](#)[Close](#)[Full Screen / Esc](#)[Printer-friendly Version](#)[Interactive Discussion](#)

spheroids because the surface area of spheroids with a given d_v increases with increasing asphericity. This effect may introduce a small uncertainty to the retrieval results for the imaginary part of the complex refractive index for those experiments where only a single impaction stage was used. Here, particles of d_v larger than $1.5 \mu\text{m}$ significantly contribute to the total dust volume concentration.

4.3 Initial approach: retrieval of both the real and imaginary part of the complex refractive index

Four quantities were independently measured for each desert dust sample in our experiments: the wavelength resolved extinction and absorption coefficients, σ_{ext} and σ_{abs} , the number size distribution, and the frequency distribution of aspect ratios. Our initial scheme to retrieve the wavelength dependent complex refractive index of the dust aerosols at each wavelength was as follows. Based on an initial guess for the real, n_{ini} , and imaginary part, k_{ini} , of the complex refractive index at a given wavelength, the size- and shape averaged extinction and absorption coefficients of the aerosol particles could be calculated from the database using the measured number size distribution and frequency distribution of aspect ratios as input, yielding the quantities $\sigma_{\text{ext,calc}}(n_{\text{ini}}, k_{\text{ini}})$ and $\sigma_{\text{abs,calc}}(n_{\text{ini}}, k_{\text{ini}})$. Then, the combined root mean square (rms) deviations between the measured quantities from LOPES and SOAP, $\sigma_{\text{ext,meas}}(n, k)$ and $\sigma_{\text{abs,meas}}(n, k)$, and the computed values could be calculated (Eq. 4).

$$\text{rms}_{\text{abs+ext}}(n, k) = \underbrace{\left[\frac{\sigma_{\text{abs,meas}}(n, k) - \sigma_{\text{abs,calc}}(n_{\text{ini}}, k_{\text{ini}})}{\sigma_{\text{abs,calc}}(n_{\text{ini}}, k_{\text{ini}})} \right]^2}_{\text{rms}_{\text{abs}}} + \underbrace{\left[\frac{\sigma_{\text{ext,meas}}(n, k) - \sigma_{\text{ext,calc}}(n_{\text{ini}}, k_{\text{ini}})}{\sigma_{\text{ext,calc}}(n_{\text{ini}}, k_{\text{ini}})} \right]^2}_{\text{rms}_{\text{ext}}} \quad (4)$$

Equation 4 holds for each wavelength step of the extinction and absorption measurements. Then, the added $\text{rms}_{\text{abs+ext}}$ value for extinction plus absorption could be minimised by optimising the initial guess values n_{ini} and k_{ini} , yielding the true values for n and k at each wavelength. Because the absorption spectrum is mainly determined by the magnitude of k , and the extinction spectrum, for weakly absorbing particles, is

Complex refractive indices of Saharan dust samples

R. Wagner et al.

Title Page

Abstract

Introduction

Conclusions

References

Tables

Figures

◀

▶

◀

▶

Back

Close

Full Screen / Esc

Printer-friendly Version

Interactive Discussion



mainly governed by the magnitude of n , the minimisation of the combined $\text{rms}_{\text{abs+ext}}$ value should yield a unique retrieval result for both n and k . To check this hypothesis we have performed the following test calculations.

Using the measured number size distribution of re-dispersed dust particles from Exp. 1 (Burkina Faso dust sample) as input, we have calculated the extinction and absorption coefficients for two wavelengths ($\lambda = 0.8$ and $0.3 \mu\text{m}$) at each point of a two-dimensional grid spanned by the real and the imaginary part of the complex refractive index, varying n between 1.3 and 1.7 and k between 0.0001 and 0.1. The computations were done for an aspect ratio of 2. We have then defined the extinction and absorption coefficients calculated for $n = 1.5$ and $k = 0.05$ as $\sigma_{\text{ext, meas}}$ and $\sigma_{\text{abs, meas}}$, thereby simulating a measurement of these quantities. Afterwards we have calculated according to Eq. (4) for all other grid points the root mean square deviations $\text{rms}_{\text{abs+ext}}$, rms_{abs} , and rms_{ext} of σ_{ext} and σ_{abs} in relation to these simulated measurements. By plotting the computed rms values as contour lines in the n and k space (Fig. 9), we can analyse whether other combinations of n and k yield the same extinction and absorption coefficients as obtained for $n = 1.5$ and $k = 0.05$, meaning that no unambiguous retrieval result for the complex refractive index can be obtained. On the contrary, a distinct global minimum in the contour plot of $\text{rms}_{\text{abs+ext}}$ at $n = 1.5$ and $k = 0.05$ would indicate that only calculations with this particular complex refractive index as input are able to simultaneously reproduce the simulated measurements of both $\sigma_{\text{ext, meas}}$ and $\sigma_{\text{abs, meas}}$.

The set of three panels in top left part of Fig. 9 shows the rms values for the computations at $\lambda = 0.8 \mu\text{m}$. The contour plot for rms_{ext} (left chart, blue lines) displays a long valley that extends over the complete range of k values whereas n only varies between about 1.525 and 1.475 along the valley floor. This means that the extinction spectrum is indeed governed by the magnitude of n and its value is fairly constrained by the extinction measurement. The opposite behaviour holds for rms_{abs} (middle chart, red lines). Here, the valley extends over the complete range of n values with k only varying between 0.04 and 0.06 along the valley floor. The absorption spectrum therefore

Complex refractive indices of Saharan dust samples

R. Wagner et al.

Title Page

Abstract

Introduction

Conclusions

References

Tables

Figures

◀

▶

◀

▶

Back

Close

Full Screen / Esc

Printer-friendly Version

Interactive Discussion



constrains the magnitude of the imaginary part of the complex refractive index. Adding the rms_{ext} and rms_{abs} values (right chart, black lines) then leads to a well defined global minimum at $n = 1.5$ and $k = 0.05$, i.e. simultaneously fitting the measured extinction and absorption coefficients at $\lambda = 0.8 \mu\text{m}$ leads to a unique retrieval result for the complex refractive index.

A different behaviour is observed for the computations at $\lambda = 0.3 \mu\text{m}$ which are shown in the set of three panels in the top right part of Fig. 9. Whereas the contour plot for rms_{abs} is similar to that at $\lambda = 0.8 \mu\text{m}$, the contour plot for rms_{ext} displays an extremely shallow, curved valley. Note that the outmost grid lines in the rms_{ext} plot correspond to a value of only 0.001 which is one order of magnitude smaller than that of the outmost grid lines shown in the contour plot of rms_{abs} . The added $\text{rms}_{\text{ext+abs}}$ contour plot is therefore dominated by the absorption contribution and reveals the characteristic long valley extending over the complete range of n values. For that reason, the magnitude of n is not constrained by simultaneous extinction and absorption measurements at $\lambda = 0.3 \mu\text{m}$. In order to understand this modified behaviour, we have plotted in the bottom panel of Fig. 9 the extinction efficiencies, Q_{ext} , as a function of the size parameter, x , for a series of complex refractive indices along the valley floor of the rms_{ext} contour plot (denoted by the coloured points). In addition, the volume size distribution of the Burkina Faso dust particles that was employed in the calculations is also shown, having been transformed to the size parameter scale for the $\lambda = 0.8 \mu\text{m}$ (circles) and $\lambda = 0.3 \mu\text{m}$ (squares) wavelengths. At $\lambda = 0.8 \mu\text{m}$, almost the entire volume size distribution is located in the size regime before the first interference maximum in the various Q_{ext} traces is reached. For these particle sizes, Q_{ext} systemically decreases with decreasing n , meaning that the magnitude of n controls the value for the size averaged extinction coefficient. Similar values for σ_{ext} are thus only obtained within a small range of n values, corresponding to the valley in the respective rms_{ext} contour plot (left chart in the top left part of Fig. 9). In contrast, at $\lambda = 0.3 \mu\text{m}$ the maximum of the volume size distribution is located in the regime of the first maximum of the extinction efficiency. As its amplitude and peak position depends on the magnitude of both n and k , different

Complex refractive indices of Saharan dust samples

R. Wagner et al.

Title Page

Abstract

Introduction

Conclusions

References

Tables

Figures

◀

▶

◀

▶

Back

Close

Full Screen / Esc

Printer-friendly Version

Interactive Discussion



combinations of the real and the imaginary part of the complex refractive index may accidentally yield the same size averaged value for σ_{ext} . When analysing e.g. the black and red traces in the bottom panel of Fig. 9, the first interference maximum is shifted to a larger x for the computation with $n = 1.41$ and $k = 0.01$ compared to that with $n = 1.69$ and $k = 0.058$. Both traces first intersect at about $x = 4.5$ which roughly corresponds to the centre of the volume size distribution of the dust particles. One part of the particle volume is therefore located in a size range corresponding to the extinction maximum of the black trace, and the other half is located in a size range that features the extinction maximum of the red trace, thus overall leading to the same size averaged extinction coefficient for both complex refractive indices.

The test calculations shown in Fig. 9 were done for an aerosol number size distribution typically generated when using two impaction stages of the cyclone system. The pronounced global minimum in the $\text{rms}_{\text{abs+ext}}$ contour plot (right chart in the top left part) is conserved down to a wavelength of about 500 nm. Unique retrieval results for both n and k should therefore be obtained at visible wavelengths but not towards the UV spectral region. The situation is worse for the experiments with just a single impaction stage. Here, a larger fraction of the dust volume concentration is located in the size regime of the first interference maximum already at $\lambda = 0.5 \mu\text{m}$, thereby not enabling a unique retrieval of both n and k . We have therefore devised an alternative retrieval approach as outlined in the following section.

4.4 Modified retrieval approach: optimising the measured number size distributions of the dust particles

In contrast to the imaginary part of the complex refractive index, the real part of the mineral dust refractive index usually shows less variation with the wavelength in the visible spectral regime. Petzold et al. (2009), for example, have derived almost constant n values between 1.55 and 1.56 from the analysis of the PSAP data during SAMUM-1. Kandler et al. (2009) report a slight increase of n towards UV wavelengths, yielding $n = 1.582$ at 350 nm as volume-weighted average. Based on previous data from the

Complex refractive indices of Saharan dust samples

R. Wagner et al.

Title Page

Abstract

Introduction

Conclusions

References

Tables

Figures



Back

Close

Full Screen / Esc

Printer-friendly Version

Interactive Discussion



literature, Müller et al. (2009) have assumed the real part of the complex refractive index to be 1.53, independent of the wavelength, in order to correct the SOAP absorption measurements for scattering. AERONET retrievals for different desert dust sites have yielded n values ranging from 1.48 to 1.56 (Dubovik et al., 2002a). Addressing our retrieval problem described in the previous section, we might therefore prescribe the n value at shorter wavelengths to that deduced at longer wavelengths where a unique retrieval result for both n and k could still be obtained. At shorter wavelengths, only the imaginary part of the complex refractive index would then be retrieved from the absorption spectrum using the measured number size distribution as input.

When deducing the n and k values for the different desert dust samples at longer wavelengths, however, we have observed a significant spread in the averaged n values that were computed from the set of three to four individual measurements performed during each experiment listed in Table 1. Even for the three samples SAMUM B1, B2, and B3 which have a similar mineralogical composition, the deduced averaged n values were in the range from 1.35 to 1.65. Since this variation is much larger than that expected from previous literature studies and the mineralogical composition as described above, we attribute it to uncertainties in the size distribution measurements, induced e.g. by inaccurate choices for χ and ρ_P from Eq. (1) to combine the SMPS and APS data. These inherent uncertainties associated with the sizing of the dust particles, which are also well-documented in the literature (Reid et al., 2003), would then directly affect the accuracy of the retrievals for the imaginary part k of the complex refractive index. We have addressed this problem as follows.

We chose to prescribe the real part of the complex refractive index to a constant value for all wavelengths in the UV-VIS spectral region. Thereby, the measurement of the extinction spectrum with LOPES became obsolete in the retrieval because only the absorption spectrum measured with SOAP was still needed to deduce the imaginary part of the complex refractive index. We therefore used the extinction spectrum as input for optimising the measured number size distribution of the dust particles. For this purpose, each measured number size distribution was first fitted by two or three

Complex refractive indices of Saharan dust samples

R. Wagner et al.

Title Page

Abstract

Introduction

Conclusions

References

Tables

Figures

◀

▶

◀

▶

Back

Close

Full Screen / Esc

Printer-friendly Version

Interactive Discussion



log-normal modes (step 1 in the retrieval flowchart shown in Fig. 10). We have then calculated the size-averaged extinction spectrum for the fitted number size distribution from the pre-computed look-up tables, using, as stated above, a constant value for n and an initial guess for the wavelength-dependent k spectrum (step 3). The latter was retrieved from the measured absorption spectrum using the fitted number size distribution as input, i.e. for each wavelength step of the SOAP absorption measurement, k was optimised to minimise the root-mean square deviation between the measured absorption coefficient and the size-averaged value computed from the look-up tables for a fixed n (step 2). Afterwards, the parameters of the two or three individual log-normal modes (number concentration, mode width, and count median diameter) of the dust particle number size distribution were optimised to obtain best agreement between the measured and the computed extinction spectrum (step 4). The total number concentration, however, was prescribed to that measured with the condensation particle counter, i.e. only the distribution of the total dust particle number concentration amongst the two or three individual modes was varied. The modified number size distribution from this first iteration step was used to obtain an improved guess for the k spectrum (step 2), which then was used to further optimise the number size distribution in second iteration steps 3 and 4 (Fig. 10). In all these steps, the downhill simplex method was used as the optimisation technique (Press et al., 1992).

Figure 11 shows exemplary results of the outlined retrieval procedure for Exp. 8 (SAMUM B3 sample, two impaction stages, see also Fig. 2), underlining one key issue that we have not addressed so far, namely the dependency of this approach on the shape of the particles. The left panel contains the measured extinction spectrum (black line) and various best fitted extinction spectra (coloured lines) for different assumptions on the value for the wavelength independent real part of the complex refractive index and for the aspect ratio of the dust particles. The right panel depicts the measured number size distribution from the combination of SMPS and APS (black squares) and the optimised number size distributions that yielded the computed extinction spectra shown in the left panel (same colour code). Also denoted in the right panel are the

Complex refractive indices of Saharan dust samples

R. Wagner et al.

[Title Page](#)[Abstract](#)[Introduction](#)[Conclusions](#)[References](#)[Tables](#)[Figures](#)[◀](#)[▶](#)[◀](#)[▶](#)[Back](#)[Close](#)[Full Screen / Esc](#)[Printer-friendly Version](#)[Interactive Discussion](#)

Complex refractive indices of Saharan dust samples

R. Wagner et al.

Title Page

Abstract

Introduction

Conclusions

References

Tables

Figures

◀

▶

◀

▶

Back

Close

Full Screen / Esc

Printer-friendly Version

Interactive Discussion



total dust volume concentrations, V , for the various fit scenarios. The red, green, and blue traces all correspond to calculations for elongated dust particles with an aspect ratio of $\varepsilon = 0.25$ but choosing different values for n , thereby covering the variability of this quantity that has been observed in previous studies. For this particle shape, the measured number size distribution, in particular for $n = 1.53$ (red line) and $n = 1.47$ (blue line), only needs to be slightly modified to obtain a very good agreement between the computed and the measured extinction spectrum. Introducing an absolute uncertainty of 0.06 in the magnitude of the n value with respect to $n = 1.53$, i.e. $n = 1.53 \pm 0.06$, leads to a change in V of at most 15%. Since V determines the magnitude of the imaginary part of the complex refractive index, the retrieval results for the k spectrum will be affected by the same uncertainty.

The two further coloured lines in Fig. 11 correspond to fit results for spherical particles with $\varepsilon = 1$. The brown line in the left panel shows the extinction spectrum of the dust particles for the initially fitted, i.e. not yet optimised number size distribution. Apparently, a spherical particle shape greatly fails to reproduce the measured habitus of the extinction spectrum for a size distribution that is similar to the measured one. In particular, the continuous increase in the extinction coefficient towards UV wavelengths is not mimicked by the spherical particles. The computed extinction spectrum, in the direction from longer to shorter wavelengths, can be regarded as an image of the trace of the extinction efficiency with increasing size parameter (see right panel of Fig. 8). The maximum of the extinction coefficient at about 400 nm for the $\varepsilon = 1$ computations thereby reflects the pronounced first interference maximum in the Q_{ext} curve. This maximum is absent in the $\varepsilon = 0.25$ computations because the interference structure is distorted so that the first maximum is shifted to larger size parameters. An elongated spheroid is obviously a much more suited shape representation than a sphere to model the extinction coefficients of dust particles with sizes that partly extend into the regime that is governed by the interference structure. As already highlighted in Sect. 4.2, the trace for C_{ext} of the $\varepsilon = 0.25$ spheroid closely agrees with that of the aggregate particle (see left panel of Fig. 8) up to a diameter d_v of about 1.1 μm , i.e. for the complete range

of particle sizes covered by the experiment (see right panel of Fig. 11). This underlines that an aggregate like shape is indeed a good proxy for calculating the extinction cross sections of the re-dispersed dust particles in our experiments.

The second fit example for $\varepsilon = 1$ which is shown in Fig. 11 (magenta line) represents the optimised number size distribution after two overall iteration steps. It is obvious that the measured number size distribution has to be significantly distorted in order to obtain a reasonable agreement between the measured and the computed extinction spectrum for $\varepsilon = 1$. In a recent environmental aerosol chamber study on the extinction spectra of key components of mineral dust aerosol, Mogili et al. (2007) have observed an excellent agreement between measured extinction spectra in the UV-VIS spectral range and those calculated from Mie theory simulations. The retrieved log-normal number size distributions, however, were not compared to independent measurements. Thus, likewise to the optimised number size distribution for $\varepsilon = 1$ in our study, the true number size distributions of the samples investigated by Mogili et al. (2007) might also have been deformed to obtain the good agreement between the measured extinction data and the Mie-based simulations.

Note that the total volume concentration of the dust aerosol inferred from the optimised number size distribution for $\varepsilon = 1$ deviates by less than 10 % from that calculated for the $\varepsilon = 0.25$ fit. Independent of the choice of the aspect ratio that is employed in the optimising approach, the overall aerosol volume concentration and the retrieved wavelength-dependent k spectrum are thus only affected by a small uncertainty. We have therefore optimised the measured number size distributions for all experiments using prolate spheroids with $\varepsilon = 0.25$ as the particle shape. Comparisons between the measured and the optimised number size distribution for experiments with the four other dust samples are compiled in Fig. 12. Like in Müller et al. (2009), we have used $n = 1.53$ for all these calculations (WMO, 1986). As outlined above, the retrieval of the spectrum of the imaginary part of the complex refractive index from the absorption measurement with SOAP was already inherent in the iterative approach (step 2, Fig. 10). The retrieved k data sets will be presented and discussed in the next section.

Complex refractive indices of Saharan dust samples

R. Wagner et al.

Title Page

Abstract

Introduction

Conclusions

References

Tables

Figures

◀

▶

◀

▶

Back

Close

Full Screen / Esc

Printer-friendly Version

Interactive Discussion



Complex refractive indices of Saharan dust samples

R. Wagner et al.

Title Page

Abstract

Introduction

Conclusions

References

Tables

Figures

◀

▶

◀

▶

Back

Close

Full Screen / Esc

Printer-friendly Version

Interactive Discussion



As emphasised in the context of the shape-dependent calculations of C_{abs} shown in the bottom panel of Fig. 8, the choice of ε does not influence the k retrievals for experiments where two impactation stages were used. For experiments 2 and 9 with a single impactation stage (Table 1), a part of the dust size distribution is located in a regime where the absorption cross sections become slightly dependent on the particle shape. It cannot be proven whether the $\varepsilon = 0.25$ spheroid is also the best shape representative for the absorption properties of the dust particles. We nevertheless strongly assume that the larger surface area of these elongated spheroids also better represents the actual surface area of the irregularly formed dust grains than the smaller surface area of the comparatively compactly shaped spheroidal shapes that are obtained by fitting ellipses to the projected particle areas in the SEM image analyses. For these two experiments, we have additionally used the shape distributions inferred from the SEM images together with the optimised number size distributions to retrieve the k spectrum from the absorption measurements. The deviations from these k retrievals to those for the fixed $\varepsilon = 0.25$ shape were less than 5%.

5 Results and discussion

5.1 Overview: the retrieved spectra of the imaginary part of the complex refractive index

Figure 13 shows a compilation of our retrieval results for the spectra of the imaginary part of the complex refractive index of the various re-dispersed Saharan soil samples. To illustrate the degree of variation in the retrieval results, the upper two panels depict all individual k spectra that were deduced from repetitive synchronised measurements of the extinction and the absorption spectrum as well as the number size distribution within experiment series conducted with the SAMUM B3 and Cairo 2 soil samples. Mean k spectra and their standard error, as calculated from all individual measurements, are shown in red. Concerning the results for the SAMUM B3 sample, no systematic deviation between the k spectra from the experiment series with one

and two impaction stages can be observed. The same behaviour was found for the two respective experiment series with the Burkina Faso soil sample. A potential size dependence of the refractive index for $<1\ \mu\text{m}$ and $>1\ \mu\text{m}$ sized dust grains (see Fig. 2) is therefore too small to be resolved within the accessible accuracy of our measurements and retrieval approach.

In the bottom panel of Fig. 13, all mean k spectra of the five investigated dust samples are compared. All dust aerosols feature a low, constant background absorption value for wavelengths larger than about 600 nm. This background level is between 0.002 and 0.003 for the Burkina Faso, Cairo 2, and SAMUM B3 dust samples whereas it is clearly increased to about 0.005 for the SAMUM B1 and SAMUM B2 samples. It is important to clarify whether this difference is an intrinsic property of the dust samples or whether it might be explained by measurement uncertainties. The two upper panels of Fig. 13 underline the good reproducibility of the individual k retrievals from the SOAP measurements over the entire wavelength range. It should be noted, however, that the SOAP data are affected by a higher uncertainty in spectral regimes where light absorption is low, because, under such conditions, the measured absorption coefficients are of similar magnitude as the cross sensitivity to scattering (Sect. 2.2). Therefore, it is useful to compare the SOAP measurements with the records from the four wavelengths photo acoustic spectrometer ($4\lambda - \text{PAS}$) that has no cross sensitivity to particle scattering. Such a comparison is shown in Fig. 14 for individual absorption measurements of the re-dispersed SAMUM B2 and Cairo 2 dust samples. Note that a detailed inter-comparison of the two techniques for measuring particle absorption which would also help to better constrain their respective measurement uncertainties is beyond the scope of the present manuscript. The important outcome from the comparison shown in Fig. 14 for our current investigation is that both absorption measurements reflect the clearly higher background absorption level at $\lambda > 600\ \text{nm}$ of the SAMUM B2 compared to the Cairo 2 dust sample. The spread in the k retrievals for $\lambda > 600\ \text{nm}$ therefore seems to reflect the actual variability of the background absorption level of the various re-dispersed Saharan soil samples.

Complex refractive indices of Saharan dust samples

R. Wagner et al.

Title Page

Abstract

Introduction

Conclusions

References

Tables

Figures

◀

▶

◀

▶

Back

Close

Full Screen / Esc

Printer-friendly Version

Interactive Discussion



Below 600 nm, k starts to increase steadily towards the UV regime for all dust probes. The outstanding role of the reddish brown coloured Burkina Faso dust sample in comparison with the other four yellow brown coloured soil samples immediately becomes obvious. Towards UV wavelengths, the value for k increases up to about 0.05 for the re-dispersed Burkina Faso soil sample whereas maximum values between 0.016 and 0.022 are reached for the other dust types. Table 5 contains a compilation of the retrieved k values at some selected wavelengths. The 600 nm threshold corresponds to the onset of absorption in hematite (Sokolik and Toon, 1999). It therefore seems reasonable to relate the variations in the k spectra of the different dust samples to their varying hematite content (see Sects. 3.2 and 3.3). In the next section, we investigate how accurately the retrieved k spectra can be mimicked by employing mixing rule approaches using the hematite contents derived from the single particle analyses of the mineralogical composition as input. We further compare our deduced k data sets to those recently published in the literature.

5.2 Discussion: comparison with literature data and mixing-rule approaches

When comparing our retrieved k data sets with previous literature results, it should be kept in mind that our data represent effective values for entire dust particle populations that were obtained by re-dispersing various soil samples from specific geographic locations. This is because our T-matrix model has treated the particles as being homogeneous although the exemplarily shown TEM image in Fig. 5 underlines the high complexity of the internal particle structure. We also assumed that the refractive index is size-independent for a given measurement. The comparison with other laboratory studies where e.g. powder samples were employed to retrieve k by diffuse reflectance (Sokolik et al., 1993) only has limited significance because our mineralogical analyses have clearly evidenced the difference in the composition between the bulk samples (20–75 μm sieved fraction) and the air-borne particles. Two major uncertainties arise when comparing our k spectra to those retrieved during field campaigns like SAMUM-1, even if the latter took place in the source region where some of our dust

Complex refractive indices of Saharan dust samples

R. Wagner et al.

Title Page

Abstract

Introduction

Conclusions

References

Tables

Figures

◀

▶

◀

▶

Back

Close

Full Screen / Esc

Printer-friendly Version

Interactive Discussion



5 samples were collected. First, the re-dispersion of a sieved fraction of the soil samples with the inclusion of impactation stages will not entirely reproduce the size distribution of the atmospheric dust load. Secondly, even for field measurements in a source region of mineral dust, a correction for soot is necessary to infer the refractive indices of the pure dust mode because strongly absorbing soot particles, even if only present in small amounts, might significantly contribute to the k value of the total aerosol (Müller et al., 2009). This soot correction, however, is affected by a high degree of uncertainty.

10 Figure 1 in Sokolik et al. (1993) shows a collection of k spectra for dust samples from different geographical regions which were deduced by various methods. The long-wavelength background absorption level at 1000 nm varies between about $k = 0.003$ and 0.007. Towards UV wavelengths, the reported imaginary indices increase to about $k = 0.008$ –0.025 at 300 nm. Our own data for the Cairo 2 and the three SAMUM dust samples accurately fit into these k regimes whereas the Burkina Faso dust sample with the highest hematite content obviously represents an extreme case, featuring k values towards UV wavelengths which are higher than all data shown in the Sokolik et al. (1993) collection. Retrievals of k from the worldwide AERONET network for typical dust sites show much lower imaginary refractive indices with k not exceeding 0.003 at 440 nm (Dubovik et al., 2002a). Balkanski et al. (2007) have addressed this difference and argued that dust absorption at visible wavelengths might be lower than previously thought because mixing rule calculations with a hematite content of 1.5 vol%, supposed to be representative for median dust absorption, showed a very good agreement with the AERONET measurements. As will be discussed later in this section, however, the results of these calculations will strongly depend on which tabulated values for the hematite refractive index are employed. In Fig. 15, we show our retrieved k spectrum for the Burkina Faso dust sample and the averaged k data set for the three SAMUM dust samples in comparison with spectra retrieved during the SAMUM-1 and SAMUM-2 field campaigns for typical dust cases. The latter data were taken from Fig. 8 in Müller et al. (2011). Given the limitations of such a comparison as discussed above, the k data set deduced during the SAMUM-1 field campaign and

Complex refractive indices of Saharan dust samples

R. Wagner et al.

Title Page

Abstract

Introduction

Conclusions

References

Tables

Figures

◀

▶

◀

▶

Back

Close

Full Screen / Esc

Printer-friendly Version

Interactive Discussion



Complex refractive indices of Saharan dust samples

R. Wagner et al.

Title Page

Abstract

Introduction

Conclusions

References

Tables

Figures

◀

▶

◀

▶

Back

Close

Full Screen / Esc

Printer-friendly Version

Interactive Discussion



representing the atmospheric dust load shows a reasonable agreement with the averaged refractive indices of the three re-dispersed soil samples collected in the source region. The SAMUM-2 dust case shows higher k values than SAMUM-1. As indicated in the introduction, the aerosol probed during SAMUM-2 was transported over long distances to the Cape Verde islands and represents a complex mixture of dust and other compounds (soot, sulphate, sea-salt; Kandler et al., 2011; Lieke et al., 2011) where it is not possible to infer the pure dust contribution (Müller et al., 2011). The Burkina Faso k data set can obviously be regarded as the upper limit of dust absorption at wavelengths below about 550 nm.

The single particle analyses of the re-dispersed SAMUM B3, SAMUM B1, and Burkina Faso soil samples has yielded hematite volume abundances between 1.1 and 2.7%. The approximately doubled hematite content of the Burkina Faso compared to the SAMUM dust particles is nicely reflected by the two-fold difference in their absorption potential below 500 nm (Fig. 15). Note again that based on the bulk analyses discussed in Sect. 3.2, a much larger difference would have been predicted (Table 3). Using a mineralogical database, Balkanski et al. (2007) have identified hematite volume abundances of 0.9 and 2.7% as low and high hematite contents of mineral aerosol, respectively, arguing that this range is also in accordance with estimates of iron oxides in dust samples by Lafon et al. (2004) and Linke et al. (2006). We are therefore confident that the variety of dust samples that were probed in our study reasonably bracket the range of hematite amounts in atmospheric dust aerosols.

In the remaining part of the discussion, we want to compare our retrieved k data sets to those calculated with various mixing rule approaches for the hematite contents deduced from the single particle analyses. Before showing our results, we want to emphasise that we consider these mixing rule calculations not as a stringent test for verification of our retrieval results. Instead, it is rather a sensitivity study for the applicability of the mixing rule approach to reproduce effective refractive index data sets of mineral dust aerosols because we identify at least three major uncertainties that are associated with this method:

(i) The hematite volume abundance that is employed in the mixing rule calculations can only be approximately inferred from the SEM analyses because an average value for the ratio hematite to total iron has to be assumed (see Sect. 3.3). Also the amount of another potentially light absorbing mineral, namely goethite, remains unspecified. Based on the optical properties measured by Bedidi and Cervelle (1993), however, goethite has a clearly lower absorption potential than hematite at wavelengths below 600 nm.

(ii) The tabulated complex refractive indices for hematite show a huge variation; see e.g. Table 1 in Meland et al. (2011). At wavelengths below 600 nm, the k values from Bedidi and Cervelle (1993) which were employed in the mixing rule calculations by Balkanski et al. (2007) are more than a factor of two smaller than those used by Sokolik and Toon (1999), adapted from an earlier work by Query (1987). Meland et al. (2011) have observed best agreement between theoretical scattering simulations and experimental scattering data for hematite aerosol particles at wavelengths below 600 nm for simulations based on the Query (1987) data. As in Kandler et al. (2009), we therefore used the Query (1987) refractive indices for our mixing rule calculations. An averaged data set of refractive indices was calculated from the e -ray and o -ray optical constants with a 1/3 to 2/3 weighting.

(iii) A simplified mixing rule model that, e.g. applies to an entirely randomly inhomogeneous medium like the Bruggeman approximation (Bohren and Huffman, 1983), will only be a rough representation of the complex internal structure of a dust particle (Fig. 5). Similar to Sokolik and Toon (1999), we have employed the volume mean approximation as well as two effective medium theories, the Maxwell-Garnett and the Bruggeman approximations in our simulations. Sokolik and Toon (1999) have shown that both effective medium theories give similar results for the imaginary indices of two-component mixtures of quartz and hematite whereas maximum deviations of more than 80 % are obtained between

Complex refractive indices of Saharan dust samples

R. Wagner et al.

[Title Page](#)[Abstract](#)[Introduction](#)[Conclusions](#)[References](#)[Tables](#)[Figures](#)[◀](#)[▶](#)[◀](#)[▶](#)[Back](#)[Close](#)[Full Screen / Esc](#)[Printer-friendly Version](#)[Interactive Discussion](#)

the computed k values from the volume mean and the Bruggeman approximation for aggregates made of 99 % quartz and 1 % hematite at a wavelength of 500 nm.

Since hematite is the only absorbing substance in the five-component model by Kandler et al. (2009) (see Table 3 therein) and because the real parts of the complex refractive index for the other four components are rather similar, we have transferred the results for the dust particle composition shown in Table 4 into a two-component model consisting of hematite and a general non-absorbing compound. For the latter, we have summed up the volume fractions of the “average silicate”, “quartz”, “calcite”, and “sulphate” components and assumed a real refractive index that linearly increases from 1.53 at 1000 nm to 1.58 at 300 nm. In the Maxwell-Garnett approximation, the non-absorbing component is treated as the homogeneous matrix where spherical hematite inclusions are embedded. In the Bruggeman approximation, both components are treated symmetrically. We employed the formulae given in Sokolik and Toon (1999) for our calculations. Figure 16 compares our retrieved k spectra for the Burkina Faso, SAMUM B1, and SAMUM B3 dust particles with those computed using the two effective medium theories and the volume mean approximation. As reported by Sokolik and Toon (1999), the computed k values from the Maxwell-Garnett and Bruggeman approximations closely agree whereas the results from the volume mean approximation are much higher with maximum deviations of almost 100 % at 500 nm. The mixing rule calculations do not reproduce the retrieved background absorption level at wavelengths larger than 600 nm, as particularly evident for the SAMUM B3 dust particles. On the one hand, some mineral components of the dust samples apart from hematite might feature such a low absorption background that is not properly described by the tabulated refractive index data. On the other, the dust samples with the elevated background absorption level might contain an additional, non-mineral compound that shows a spectrally flat absorption (Müller et al., 2011).

Between 600 and 400 nm, the retrieved k values are within the regime spanned by the volume mean and the effective medium approximations. Towards the UV regime below $\lambda = 400$ nm, the increase of k in the mixing rule calculations starts to level off

Complex refractive indices of Saharan dust samples

R. Wagner et al.

Title Page

Abstract

Introduction

Conclusions

References

Tables

Figures

◀

▶

◀

▶

Back

Close

Full Screen / Esc

Printer-friendly Version

Interactive Discussion



Complex refractive indices of Saharan dust samples

R. Wagner et al.

[Title Page](#)[Abstract](#)[Introduction](#)[Conclusions](#)[References](#)[Tables](#)[Figures](#)[⏪](#)[⏩](#)[◀](#)[▶](#)[Back](#)[Close](#)[Full Screen / Esc](#)[Printer-friendly Version](#)[Interactive Discussion](#)

whereas the retrieved k values, in particular for the Burkina Faso and the SAMUM B3 sample, continue to increase in the retrieved data sets. A variety of explanations could account for this behaviour, including a higher uncertainty of the SOAP measurements towards UV wavelengths, errors in the tabulated refractive indices for hematite, or the onset of absorption by other mineral constituents in this spectral regime. The variability of the individual retrieval runs, as expressed by the error bars, is much lower than the sensitivity to the mixing state. This underlines our initial statement that these calculations are not suited to assess the accuracy of the deduced k spectra. Note that our computed k values are much higher than those from the mixing rule calculations by Balkanski et al. (2007) (see Figs. 3 and 4 therein) although similar volume fractions of hematite were employed. This difference is solely related to the variations in the tabulated refractive indices for hematite.

6 Summary

Five different Saharan soil samples of variable mineralogical composition were re-dispersed into an aerosol chamber yielding number size distributions with median dust particle diameters of typically 0.3–0.4 μm and upper particle diameters in the range from 2 to 4 μm , depending on the number of impaction stages that were used during aerosol generation. The extinction and absorption coefficients as well as the number size distribution of the dust particles were simultaneously measured with various techniques to retrieve their complex refractive indices at wavelengths between 305 and 955 nm with an inversion scheme based on a spheroidal dust model. Since previous literature studies have revealed that the real part of the complex refractive index of dust aerosols is rather constant over the considered spectral range, its value was fixed to 1.53. The extinction spectra were used as reference measurements to optimise the simultaneously recorded number size distributions of the dust particles. Thereby, the inherent uncertainties associated with the sizing of dust which are caused, e.g. by corrections needed to account for the asphericity of the particles, could be reduced. We

Complex refractive indices of Saharan dust samples

R. Wagner et al.

[Title Page](#)[Abstract](#)[Introduction](#)[Conclusions](#)[References](#)[Tables](#)[Figures](#)[⏪](#)[⏩](#)[◀](#)[▶](#)[Back](#)[Close](#)[Full Screen / Esc](#)[Printer-friendly Version](#)[Interactive Discussion](#)

have shown that computations for elongated dust spheroids of aspect ratio 0.25 best fitted the measured extinction spectra whereas calculations for dust spheres did not accurately reproduce the observed spectral habitus. The optimised number size distributions were then used to derive the effective, wavelength-resolved imaginary parts of the complex refractive index of the dust aerosols from the measured absorption coefficients. This retrieval step proved to be almost insensitive to the shape of the dust particles.

The retrieved data sets of the imaginary part of the complex refractive index were analysed in terms of the hematite content of the dust aerosols because this mineral features the largest absorption potential at visible and UV wavelengths. The hematite content was inferred from single particle analyses using electron microscopy. These analyses proved to be indispensable because we have found that the mineralogical composition of the airborne particles clearly deviated from the bulk composition of the soil samples. The volume fraction of hematite in the dust aerosols varied between 1.1 and 2.7 % and is in good agreement with the range of hematite contents that are assumed to be representative of atmospheric dust aerosols. Therefore, our retrieved k data sets are valuable to constrain the range of variability of the absorption potential of airborne dust particles.

At wavelengths larger than 600 nm, i.e. above the onset of dust absorption due to hematite, the retrieved k values varied between 0.003 and 0.005. At 505 nm, k increased to 0.005–0.011 and a range of k values between 0.016 and 0.050 was observed in the UV regime at 305 nm. The highest k values, retrieved for a reddish brown coloured dust sample from Burkina Faso, were considered as an upper limit for the absorption potential of atmospheric dust aerosols. The averaged k data set of three yellow brown coloured, re-dispersed soil samples that were collected in southern Morocco during the SAMUM-1 field campaign showed a good agreement with the k values deduced from the field measurements for a typical dust case. In a sensitivity study, we have investigated how accurately the retrieved k data sets could be mimicked by mixing rule approximations employing the experimentally determined hematite contents

as input. The results from these calculations are in qualitative agreement with our retrieved k values but feature a huge variation depending on which model is used to describe the mixing state of the mineral aerosols and which tabulated refractive index data set for hematite is employed.

5 *Acknowledgements.* This research was funded by the Helmholtz-Gemeinschaft Deutscher
Forschungszentren as part of the program “Atmosphere and Climate”. We thank C. Adelhelm
(Institute for Applied Materials – Applied Materials Physics, IAM-AWP, Karlsruhe Institute of
Technology) for the analyses of the elemental composition of the soil samples. A special thank
is addressed to L. Schütz (Institute for Atmospheric Physics, University of Mainz) and M. Kohler
10 (Institute for Meteorology and Climate Research – Troposphere Research, IMK-TRO, Karlsruhe
Institute of Technology) for providing the desert dust samples. We acknowledge a partial fund-
ing by the Deutsche Forschungsgemeinschaft in the frame of the SAMUM research group (FOR
539).

References

- 15 Ajtai, T., Filep, A., Schnaiter, M., Linke, C., Vragel, M., Bozoki, Z., Szabo, G., and Leisner, T.:
A novel multi-wavelength photoacoustic spectrometer for the measurement of the UV-vis-
NIR spectral absorption coefficient of atmospheric aerosols, *J. Aerosol Sci.*, 41, 1020–1029,
2010.
- Alfaro, S. C., Lafon, S., Rajot, J. L., Formenti, P., Gaudichet, A., and Maille, M.: Iron oxides and
20 light absorption by pure desert dust: An experimental study, *J. Geophys. Res.-Atmos.*, 109,
D08208, doi:10.1029/2003JD004374, 2004.
- Balkanski, Y., Schulz, M., Claquin, T., and Guibert, S.: Reevaluation of Mineral aerosol radi-
ative forcings suggests a better agreement with satellite and AERONET data, *Atmos. Chem.*
Phys., 7, 81–95, doi:10.5194/acp-7-81-2007, 2007.
- 25 Baran, A. J., and Havemann, S.: Rapid computation of the optical properties of hexagonal
columns using complex angular momentum theory, *J. Quant. Spectrosc. Ra.*, 63, 499–519,
1999.
- Baran, A. J., Francis, P. N., Havemann, S., and Yang, P.: A study of the absorption and extinction
properties of hexagonal ice columns and plates in random and preferred orientation, using

Complex refractive indices of Saharan dust samples

R. Wagner et al.

Title Page

Abstract

Introduction

Conclusions

References

Tables

Figures

◀

▶

◀

▶

Back

Close

Full Screen / Esc

Printer-friendly Version

Interactive Discussion



Complex refractive indices of Saharan dust samples

R. Wagner et al.

Title Page

Abstract

Introduction

Conclusions

References

Tables

Figures

◀

▶

◀

▶

Back

Close

Full Screen / Esc

Printer-friendly Version

Interactive Discussion



exact T-matrix theory and aircraft observations of cirrus, *J. Quant. Spectrosc. Ra.*, 70, 505–518, 2001.

Bedidi, A. and Cervelle, B.: Light-Scattering by Spherical-Particles with Hematite and Geothite-Like Optical-Properties – Effect of Water Impregnation, *J. Geophys. Res. (Sol. Ea.)*, 98, 11941–11952, 1993.

Bohren, C. F. and Huffman, D. R.: Absorption and Scattering of Light by Small Particles, John Wiley & Sons, Inc., New York, 1983.

Chung, F. H.: Quantitative Interpretation of X-Ray-Diffraction Patterns of Mixtures .1. Matrix-Flushing Method for Quantitative Multicomponent Analysis, *J. Appl. Crystallogr.*, 7, 519–525, 1974.

Claquin, T., Schulz, M., and Balkanski, Y. J.: Modeling the mineralogy of atmospheric dust sources, *J. Geophys. Res.-Atmos.*, 104, 22243–22256, 1999.

Draine, B. T. and Flatau, P. J.: Discrete-Dipole Approximation for Scattering Calculations, *J. Opt. Soc. Am. A*, 11, 1491–1499, 1994.

Dubovik, O., Holben, B., Eck, T. F., Smirnov, A., Kaufman, Y. J., King, M. D., Tanre, D., and Slutsker, I.: Variability of absorption and optical properties of key aerosol types observed in worldwide locations, *J. Atmos. Sci.*, 59, 590–608, 2002a.

Dubovik, O., Holben, B. N., Lapyonok, T., Sinyuk, A., Mishchenko, M. I., Yang, P., and Slutsker, I.: Non-spherical aerosol retrieval method employing light scattering by spheroids, *Geophys. Res. Lett.*, 29, 1415, doi:10.1029/2001GL014506, 2002b.

Dubovik, O., Sinyuk, A., Lapyonok, T., Holben, B. N., Mishchenko, M., Yang, P., Eck, T. F., Volten, H., Munoz, O., Veihelmann, B., van der Zande, W. J., Leon, J. F., Sorokin, M., and Slutsker, I.: Application of spheroid models to account for aerosol particle non-sphericity in remote sensing of desert dust, *J. Geophys. Res.-Atmos.*, 111, D11208, doi:10.1029/2005JD006619, 2006.

Fournier, G. R. and Evans, B. T. N.: Approximation to Extinction Efficiency for Randomly Oriented Spheroids, *Appl. Opt.*, 30, 2042–2048, 1991.

Hansen, J. E. and Travis, L. D.: Light-Scattering in Planetary Atmospheres, *Space. Sci. Rev.*, 16, 527–610, 1974.

Hinds, W. C.: Aerosol Technology, John Wiley & Sons, Inc., New York, 1999.

ICDD: Powder Diffraction File PDF-2, JCPDS – International Center for Diffraction Data, Newton Square, PA, USA, 2002.

Kandler, K., Benker, N., Bundke, U., Cuevas, E., Ebert, M., Knippertz, P., Rodriguez, S., Schutz,

Complex refractive indices of Saharan dust samples

R. Wagner et al.

[Title Page](#)[Abstract](#)[Introduction](#)[Conclusions](#)[References](#)[Tables](#)[Figures](#)[◀](#)[▶](#)[◀](#)[▶](#)[Back](#)[Close](#)[Full Screen / Esc](#)[Printer-friendly Version](#)[Interactive Discussion](#)

L., and Weinbruch, S.: Chemical composition and complex refractive index of Saharan Mineral Dust at Izana, Tenerife (Spain) derived by electron microscopy, *Atmos. Environ.*, 41, 8058–8074, 2007.

5 Kandler, K., Schütz, L., Deutscher, C., Ebert, M., Hofmann, H., Jäckel, S., Jaenicke, R., Knipertz, P., Lieke, K., Massling, A., Petzold, A., Schladitz, A., Weinzierl, B., Wiedensohler, A., Zorn, S., and Weinbruch, S.: Size distribution, mass concentration, chemical and mineralogical composition and derived optical parameters of the boundary layer aerosol at Tinfou, Morocco, during SAMUM 2006, *Tellus B*, 61, 32–50, 2009.

10 Kandler, K., Lieke, K., Benker, N., Emmel, C., Küpper, M., Müller-Ebert, D., Ebert, M., Scheuvsens, D., Schladitz, A., Schütz, L., and Weinbruch, S.: Electron microscopy of particles collected at Praia, Cape Verde, during the Saharan Mineral Dust Experiment: particle chemistry, shape, mixing state and complex refractive index, *Tellus B*, 63, doi:10.1111/j.1600-0889.2011.00550.x, in press, 2011.

15 Karickhoff, S. W. and Bailey, G. W.: Optical Absorption Spectra of Clay-Minerals, *Clay Clay Miner.*, 21, 59–70, 1973.

Kokhanovsky, A. A. and Zege, E. P.: Local Optical-Parameters of Spherical Polydispersions – Simple Approximations, *Appl. Opt.*, 34, 5513–5519, 1995.

Lafon, S., Rajot, J. L., Alfaro, S. C., and Gaudichet, A.: Quantification of iron oxides in desert aerosol, *Atmos. Environ.*, 38, 1211–1218, 2004.

20 Lafon, S., Sokolik, I. N., Rajot, J. L., Caquineau, S., and Gaudichet, A.: Characterization of iron oxides in mineral dust aerosols: Implications for light absorption, *J. Geophys. Res.-Atmos.*, 111, D21207, doi:10.1029/2005JD007016, 2006.

25 Lieke, K., Kandler, K., Scheuvsens, D., Emmel, C., Von Glahn, C., Petzold, A., Weinzierl, B., Veira, A., Ebert, M., Weinbruch, S., and Schütz, L.: Particle chemical properties in the vertical column based on aircraft observations in the vicinity of Cape Verde Islands, *Tellus B*, 63, in press, 2011.

Linke, C., Möhler, O., Veres, A., Mohácsi, Á., Bozóki, Z., Szabó, G., and Schnaiter, M.: Optical properties and mineralogical composition of different Saharan mineral dust samples: a laboratory study, *Atmos. Chem. Phys.*, 6, 3315–3323, doi:10.5194/acp-6-3315-2006, 2006.

30 Macke, A., Mueller, J., and Raschke, E.: Single scattering properties of atmospheric ice crystals, *J. Atmos. Sci.*, 53, 2813–2825, 1996.

Meland, B., Kleiber, P. D., Grassian, V. H., and Young, M. A.: Visible light scattering study at 470, 550, and 660 nm of components of mineral dust aerosol: Hematite and goethite, *J.*

Complex refractive indices of Saharan dust samples

R. Wagner et al.

[Title Page](#)[Abstract](#)[Introduction](#)[Conclusions](#)[References](#)[Tables](#)[Figures](#)[◀](#)[▶](#)[◀](#)[▶](#)[Back](#)[Close](#)[Full Screen / Esc](#)[Printer-friendly Version](#)[Interactive Discussion](#)

Quant. Spectrosc. Ra., 112, 1108–1118, 2011.

Meng, Z. K., Yang, P., Kattawar, G. W., Bi, L., Liou, K. N., and Laszlo, I.: Single-scattering properties of tri-axial ellipsoidal mineral dust aerosols: A database for application to radiative transfer calculations, *J. Aerosol Sci.*, 41, 501–512, 2010.

5 Merikallio, S., Lindqvist, H., Nousiainen, T., and Kahnert, M.: Modelling light scattering by mineral dust using spheroids: assessment of applicability, *Atmos. Chem. Phys.*, 11, 5347–5363, doi:10.5194/acp-11-5347-2011, 2011.

Mishchenko, M. I. and Travis, L. D.: Capabilities and limitations of a current FORTRAN implementation of the T-matrix method for randomly oriented, rotationally symmetric scatterers, *J.*

10 *Quant. Spectrosc. Ra.*, 60, 309–324, 1998.

Mishchenko, M. I., Travis, L. D., Kahn, R. A., and West, R. A.: Modeling phase functions for dustlike tropospheric aerosols using a shape mixture of randomly oriented polydisperse spheroids, *J. Geophys. Res.-Atmos.*, 102, 16831–16847, 1997.

Mogili, P. K., Yang, K. H., Young, M. A., Kleiber, P. D., and Grassian, V. H.: Environmental aerosol chamber studies of extinction spectra of mineral dust aerosol components: Broadband IR-UV extinction spectra, *J. Geophys. Res.-Atmos.*, 112, D21204, doi:10.1029/2007JD008890, 2007.

15 Moore, D. M. and Reynolds, R. C. J.: *X-Ray Diffraction and the Identification and Analysis of Clay Minerals*, Oxford University Press, Oxford, New York, 1997.

20 Müller, D., Weinzierl, B., Petzold, A., Kandler, K., Ansmann, A., Müller, T., Tesche, M., Freudenthaler, V., Esselborn, M., Heese, B., Althausen, D., Schladitz, A., Otto, S., and Knippertz, P.: Mineral dust observed with AERONET Sun photometer, Raman lidar, and in situ instruments during SAMUM 2006: Shape-independent particle properties, *J. Geophys. Res.-Atmos.*, 115, D07202, doi:10.1029/2009JD012520, 2010.

25 Müller, T., Schladitz, A., Massling, A., Kaaden, N., Kandler, K., and Wiedensohler, A.: Spectral absorption coefficients and imaginary parts of refractive indices of Saharan dust during SAMUM-1, *Tellus B*, 61, 79–95, 2009.

Müller, T., Schladitz, A., Kandler, K., and Wiedensohler, A.: Spectral particle absorption coefficients, single scattering albedos, and imaginary parts of refractive indices from ground based in-situ measurements at Cape Verde Island during SAMUM-2, *Tellus B*, doi:10.1111/j.1600-0889.2011.00572.x, accepted, 2011.

30 Otto, S., Bierwirth, E., Weinzierl, B., Kandler, K., Esselborn, M., Tesche, M., Schladitz, A., Wendisch, M., and Trautmann, T.: Solar radiative effects of a Saharan dust plume observed

Complex refractive indices of Saharan dust samples

R. Wagner et al.

[Title Page](#)[Abstract](#)[Introduction](#)[Conclusions](#)[References](#)[Tables](#)[Figures](#)[◀](#)[▶](#)[◀](#)[▶](#)[Back](#)[Close](#)[Full Screen / Esc](#)[Printer-friendly Version](#)[Interactive Discussion](#)

- during SAMUM assuming spheroidal model particles, *Tellus B*, 61, 270–296, 2009.
- Petzold, A., Rasp, K., Weinzierl, B., Esselborn, M., Hamburger, T., Dornbrack, A., Kandler, K., Schutz, L., Knippertz, P., Fiebig, M., and Virkkula, A.: Saharan dust absorption and refractive index from aircraft-based observations during SAMUM 2006, *Tellus B*, 61, 118–130, 2009.
- 5 Press, W. H., Teukolsky, S. A., Vetterling, W. T., and Flannery, B. P.: *Numerical Recipes in C: The Art of Scientific Computing*, Cambridge University Press, Cambridge, 1992.
- Querry, M. R.: *Optical constants of minerals and other materials from the millimeter to the UV*, Rep. CRDEC-CR-88009, US Army, Aberdeen, MD, 1987.
- 10 Reid, J. S., Jonsson, H. H., Maring, H. B., Smirnov, A., Savoie, D. L., Cliff, S. S., Reid, E. A., Livingston, J. M., Meier, M. M., Dubovik, O., and Tsay, S. C.: Comparison of size and morphological measurements of coarse mode dust particles from Africa, *J. Geophys. Res.-Atmos.*, 108, 8593, doi:10.1029/2002JD002485, 2003.
- Scheuvens, D., Kandler, K., Küpper, M., Lieke, K., Zorn, S., Ebert, M., Schütz, L., and Weinbruch, S.: Individual-particle analysis of airborne dust samples collected over Morocco in 2006 during SAMUM 1, *Tellus B*, 63, in press, 2011.
- 15 Schladitz, A., Müller, T., Kaaden, N., Massling, A., Kandler, K., Ebert, M., Weinbruch, S., Deutscher, C., and Wiedensohler, A.: In situ measurements of optical properties at Tinfou (Morocco) during the Saharan Mineral Dust Experiment SAMUM 2006, *Tellus B*, 61, 64–78, 2009.
- 20 Schnaiter, M., Schmid, O., Petzold, A., Fritzsche, L., Klein, K. F., Andreae, M. O., Helas, G., Thielmann, A., Gimmler, M., Möhler, O., Linke, C., and Schurath, U.: Measurement of wavelength-resolved light absorption by aerosols utilizing a UV-VIS extinction cell, *Aerosol. Sci. Tech.*, 39, 249–260, 2005.
- Sokolik, I. N. and Toon, O. B.: Incorporation of mineralogical composition into models of the radiative properties of mineral aerosol from UV to IR wavelengths, *J. Geophys. Res.-Atmos.*, 25 104, 9423–9444, 1999.
- Sokolik, I., Andronova, A., and Johnson, T. C.: Complex Refractive-Index of Atmospheric Dust Aerosols, *Atmos. Environ., Part A*, 27, 2495–2502, 1993.
- Wagner, R., Linke, C., Naumann, K. H., Schnaiter, M., Vragel, M., Gangl, M., and Horvath, H.: A review of optical measurements at the aerosol and cloud chamber AIDA, *J. Quant. Spectrosc. Ra.*, 110, 930–949, 2009.
- 30 Wiegner, M., Gasteiger, J., Kandler, K., Weinzierl, B., Rasp, K., Esselborn, M., Freudenthaler, V., Heese, B., Toledano, C., Tesche, M., and Althausen, D.: Numerical simulations of optical

properties of Saharan dust aerosols with emphasis on lidar applications, Tellus B, 61, 180–194, 2009.

WMO: World Climate Program (WCP)/IAMAP, A preliminary cloudless standard atmosphere for radiation computation, WMO, Geneva, 1986.

- 5 Yang, P., Feng, Q., Hong, G., Kattawar, G. W., Wiscombe, W. J., Mishchenko, M. I., Dubovik, O., Laszlo, I., and Sokolik, I. N.: Modeling of the scattering and radiative properties of non-spherical dust-like aerosols, J. Aerosol Sci., 38, 995–1014, 2007.

Zakharova, N. T. and Mishchenko, M. I.: Scattering properties of needlelike and platelike ice spheroids with moderate size parameters, Appl. Opt., 39, 5052–5057, 2000.

Complex refractive indices of Saharan dust samples

R. Wagner et al.

Title Page

Abstract

Introduction

Conclusions

References

Tables

Figures

⏪

⏩

◀

▶

Back

Close

Full Screen / Esc

Printer-friendly Version

Interactive Discussion



Complex refractive indices of Saharan dust samples

R. Wagner et al.

Table 1. Compilation of the initial dust particle number concentrations, N_{ini} , arithmetic averages of the number size distributions, $d_{\text{v,mean}}$ (mean particle diameter), and effective diameters (Hansen and Travis, 1974), d_{eff} , of the aerosol size distributions for all experiments with the re-dispersed Saharan soil samples.

Exp. number	sample	Number of impaction stages	$N_{\text{ini}} / \text{cm}^{-3}$	$d_{\text{v,mean}} / \mu\text{m}$	$d_{\text{eff}} / \mu\text{m}$
1	Burkina Faso	2	3400	0.31	0.47
2	Burkina Faso	1	860	0.43	0.97
3	Cairo 2	2	6200	0.35	0.54
4	Cairo 2	2	6500	0.27	0.44
5	SAMUM B1	2	4000	0.34	0.61
6	SAMUM B2	2	4700	0.35	0.49
7	SAMUM B2	2	4500	0.28	0.44
8	SAMUM B3	2	3100	0.32	0.53
9	SAMUM B3	1	1800	0.42	0.88

Title Page

Abstract

Introduction

Conclusions

References

Tables

Figures

◀

▶

◀

▶

Back

Close

Full Screen / Esc

Printer-friendly Version

Interactive Discussion



Complex refractive indices of Saharan dust samples

R. Wagner et al.

Table 2. X-ray Fluorescence Analysis of the elemental composition of the 20–75 μm size fraction of the Saharan soil samples. The results are expressed as weight percentages (wt %) of oxides. The standard deviation (sd) is also denoted.

Elements as oxides	Burkina Faso		Cairo 2		SAMUM B1		SAMUM B2		SAMUM B3	
	wt %	sd	wt %	sd	wt %	sd	wt %	sd	wt %	sd
SiO ₂	74.13	0.06	55.2	0.08	70.77	0.04	59.31	0.05	65.52	0.02
Al ₂ O ₃	14.05	0.38	7.7	0.01	8.51	0.01	14.56	0.07	10.02	0.01
CaO	0.22	0.01	24.3	0.05	7.85	0.01	8.30	0.03	7.54	0.02
MgO	< 0.1		2.9	0.03	2.90	0.01	4.38	0.03	2.55	0.01
Fe ₂ O ₃	8.39	0.02	4.5	0.02	4.01	0.01	6.33	0.10	5.19	0.04
K ₂ O	0.39	0.01	1.18	0.003	2.27	0.01	2.99	0.01	1.96	0.01
Na ₂ O	< 0.5		1.1	0.18	< 0.5		< 0.5		< 0.5	
P ₂ O ₅	0.05	0.01	0.2	0.01	0.13	0.01	0.16	0.01	0.12	0.01
TiO ₂	1.24	0.02	1.4	0.07	1.14	0.06	1.30	0.02	1.56	0.01
Loss on ignition	8.38		19.1		8.64		12.55		8.25	

[Title Page](#)
[Abstract](#)
[Introduction](#)
[Conclusions](#)
[References](#)
[Tables](#)
[Figures](#)
[◀](#)
[▶](#)
[◀](#)
[▶](#)
[Back](#)
[Close](#)
[Full Screen / Esc](#)
[Printer-friendly Version](#)
[Interactive Discussion](#)


Complex refractive indices of Saharan dust samples

R. Wagner et al.

Title Page

Abstract

Introduction

Conclusions

References

Tables

Figures

◀

▶

◀

▶

Back

Close

Full Screen / Esc

Printer-friendly Version

Interactive Discussion



Table 3. X-ray Diffraction Analysis of the mineralogical composition of the 20–75 μm size fraction of the Saharan soil samples. The results are expressed as weight percentages (wt %) of identified minerals. Note that the Cairo 2 soil sample has not been analysed. The uncertainties are 20% for the clay minerals chlorite, kaolinite, illite, and pyrophyllite, as well as 10% for all other minerals.

Mineral phases	Burkina Faso	SAMUM B1	SAMUM B2	SAMUM B3
	Quartz	52	49	31
Hematite	12	1	1	–
Goethite	3	–	–	–
Microcline	–	31	24	23
Albite	–	6	5	8
Calcite	–	6	7	4
Dolomite	–	4	–	–
Gypsum	–	–	–	8
Muscovite	8	–	–	8
Chlorite	–	1	21	4
Kaolinite	19	1	11	–
Illite	6	1	–	–
Pyrophyllite	–	–	–	2

Complex refractive indices of Saharan dust samples

R. Wagner et al.

Title Page

Abstract

Introduction

Conclusions

References

Tables

Figures

◀

▶

◀

▶

Back

Close

Full Screen / Esc

Printer-friendly Version

Interactive Discussion



Table 4. Relative volume abundance of model substances derived from single particle analysis. The particle number of SAMUM B2 was not sufficient for such an analysis.

Component	Burkina Faso	SAMUM B1	SAMUM B3
Quartz	0.004	0.012	0.006
Hematite	0.027	0.016	0.011
Calcite	0.001	0.092	0.055
Average Silicate	0.949	0.842	0.867
Sulphate	0.019	0.037	0.061

Complex refractive indices of Saharan dust samples

R. Wagner et al.

Table 5. Retrieval results for the imaginary part of the complex refractive index, k , at selected wavelengths, λ , for the five investigated Saharan dust samples. The tabulated data are mean k values from a set of individual measurements; Δk denotes their standard error.

λ nm	Burkina Faso		Cairo 2		SAMUM B1		SAMUM B2		SAMUM B3	
	k	Δk	k	Δk	k	Δk	k	Δk	k	Δk
305	0.0495	0.0092	0.0157	0.0007	0.0164	0.0020	0.0220	0.0010	0.0168	0.0010
355	0.0321	0.0024	0.0125	0.0005	0.0142	0.0013	0.0178	0.0007	0.0152	0.0008
405	0.0233	0.0014	0.0089	0.0004	0.0117	0.0010	0.0142	0.0005	0.0119	0.0006
455	0.0151	0.0009	0.0060	0.0002	0.0093	0.0007	0.0107	0.0003	0.0087	0.0004
505	0.0110	0.0006	0.0048	0.0002	0.0081	0.0005	0.0090	0.0003	0.0071	0.0003
555	0.0061	0.0003	0.0033	0.0002	0.0065	0.0004	0.0066	0.0002	0.0049	0.0002
605	0.0039	0.0003	0.0027	0.0002	0.0056	0.0002	0.0052	0.0001	0.0035	0.0002
655	0.0030	0.0003	0.0023	0.0002	0.0051	0.0002	0.0045	0.0002	0.0031	0.0002
705	0.0027	0.0003	0.0022	0.0002	0.0052	0.0003	0.0044	0.0002	0.0030	0.0002
755	0.0026	0.0003	0.0022	0.0001	0.0053	0.0002	0.0045	0.0002	0.0029	0.0001
805	0.0024	0.0003	0.0022	0.0001	0.0053	0.0002	0.0042	0.0003	0.0029	0.0001
855	0.0028	0.0003	0.0022	0.0002	0.0054	0.0002	0.0045	0.0003	0.0031	0.0002
905	0.0027	0.0004	0.0022	0.0002	0.0056	0.0002	0.0045	0.0004	0.0032	0.0002
955	0.0028	0.0003	0.0021	0.0002	0.0057	0.0003	0.0042	0.0006	0.0030	0.0001

Title Page

Abstract

Introduction

Conclusions

References

Tables

Figures

⏪

⏩

◀

▶

Back

Close

Full Screen / Esc

Printer-friendly Version

Interactive Discussion



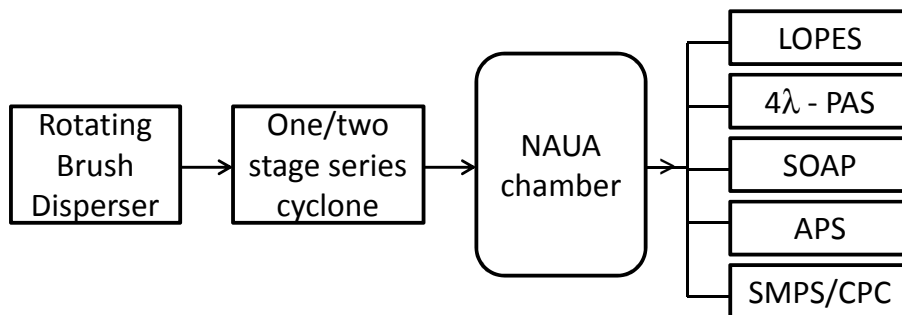


Fig. 1. Schematic set-up of the NAUA chamber experiments with re-dispersed Saharan soil samples, including aerosol generation and characterisation by LOPES (Long-path Extinction Spectrometer), 4λ - PAS (four wavelength photo acoustic spectrometer), SOAP (Spectral Optical Absorption Photometer), APS (Aerodynamic Particle Sizer), and SMPS/CPC (Scanning Mobility Particle Sizer, Condensation Particle Counter).

Complex refractive indices of Saharan dust samples

R. Wagner et al.

Title Page

Abstract Introduction

Conclusions References

Tables Figures

◀ ▶

◀ ▶

Back Close

Full Screen / Esc

Printer-friendly Version

Interactive Discussion



Complex refractive indices of Saharan dust samples

R. Wagner et al.

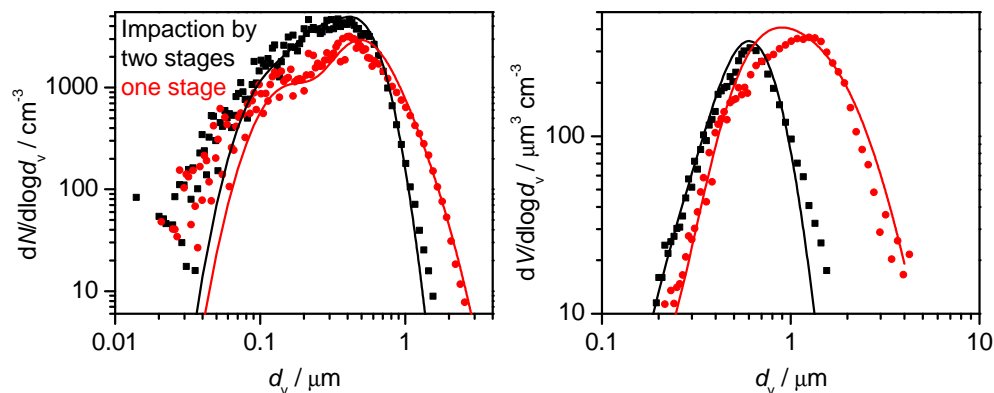


Fig. 2. Number (left panel) and volume (right panel) size distribution of re-dispersed SAMUM B3 dust particles. The black squares and red dots denote the combined SMPS/APS measurements for experiments with two stages (Exp. 8, Table 1) and one stage (Exp. 9) of the cyclone impaction system, respectively. The solid lines are the optimised size distributions obtained by best fitting the simultaneously recorded extinction spectra of the dust particles as described in Sect. 4.4.

[Title Page](#)[Abstract](#)[Introduction](#)[Conclusions](#)[References](#)[Tables](#)[Figures](#)[◀](#)[▶](#)[◀](#)[▶](#)[Back](#)[Close](#)[Full Screen / Esc](#)[Printer-friendly Version](#)[Interactive Discussion](#)

Complex refractive indices of Saharan dust samples

R. Wagner et al.

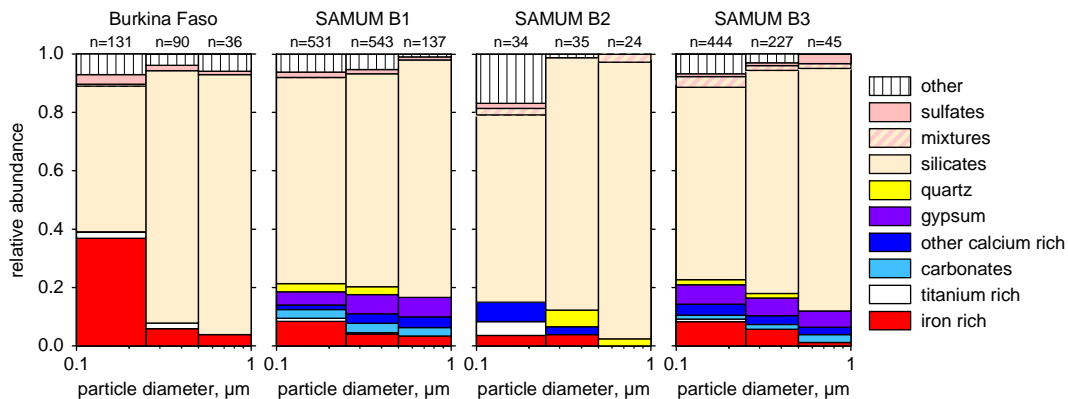


Fig. 3. Size-resolved composition of the re-dispersed soil samples. The numbers above the single bars show the number of analysed single particles in this size interval. Particles are weighted according to their volume inside the single size intervals.

Title Page

Abstract

Introduction

Conclusions

References

Tables

Figures

◀

▶

◀

▶

Back

Close

Full Screen / Esc

Printer-friendly Version

Interactive Discussion



Complex refractive indices of Saharan dust samples

R. Wagner et al.

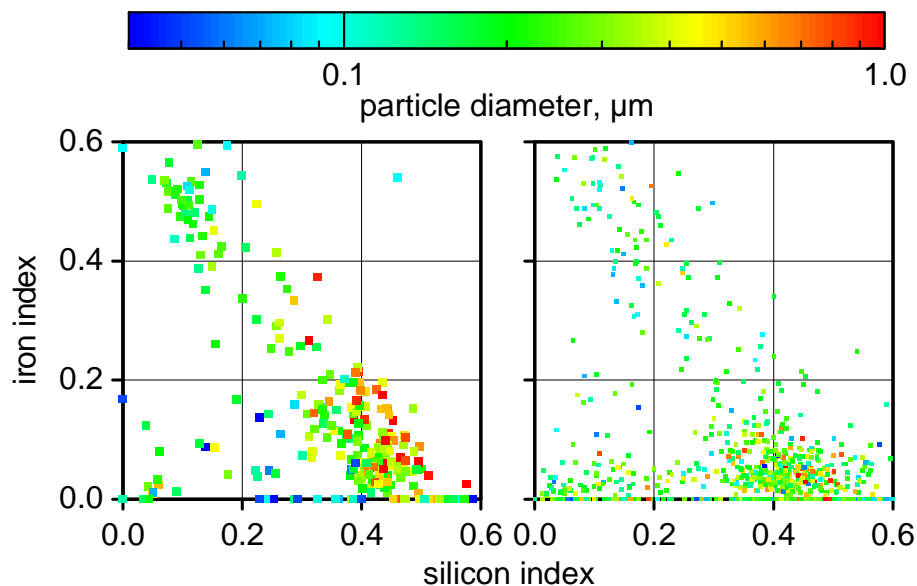


Fig. 4. Iron index versus silicon index for the Burkina Faso (left) and SAMUM B3 (right) samples. Particle diameter is coded as symbol colour. Element indices are defined as atomic ratio of the element to the sum of Na, Mg, Al, Si, P, S, Cl, K, Ca, Ti, and Fe.

Title Page

Abstract

Introduction

Conclusions

References

Tables

Figures

◀

▶

◀

▶

Back

Close

Full Screen / Esc

Printer-friendly Version

Interactive Discussion



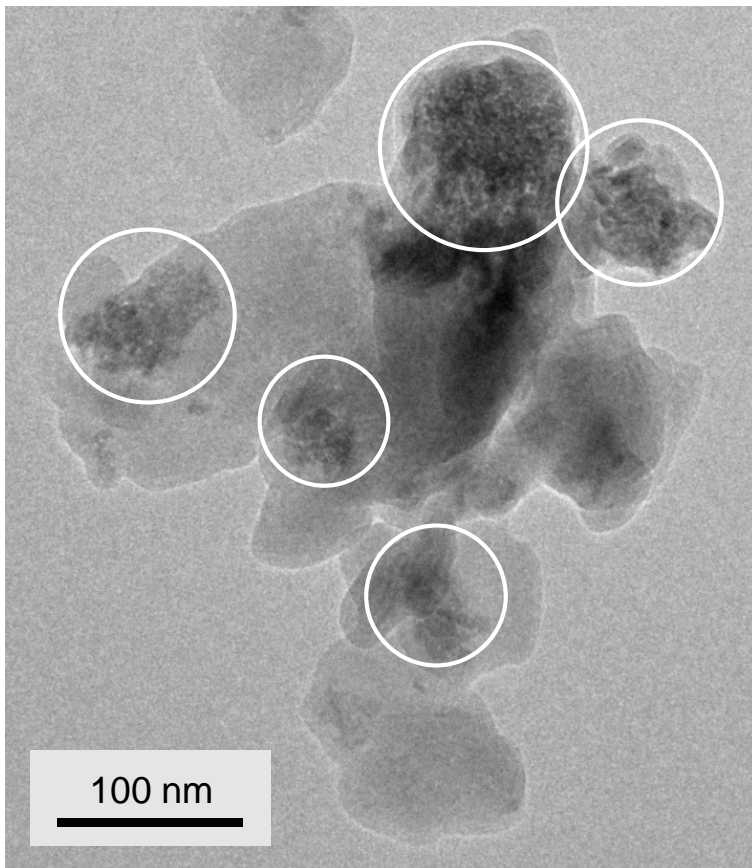


Fig. 5. Transmission electron microscopy bright-field image of a silicate particle with grains of nanometre-sized crystallites of iron oxides (marked by white circles).

Complex refractive indices of Saharan dust samples

R. Wagner et al.

Title Page

Abstract

Introduction

Conclusions

References

Tables

Figures

◀

▶

◀

▶

Back

Close

Full Screen / Esc

Printer-friendly Version

Interactive Discussion



Complex refractive indices of Saharan dust samples

R. Wagner et al.

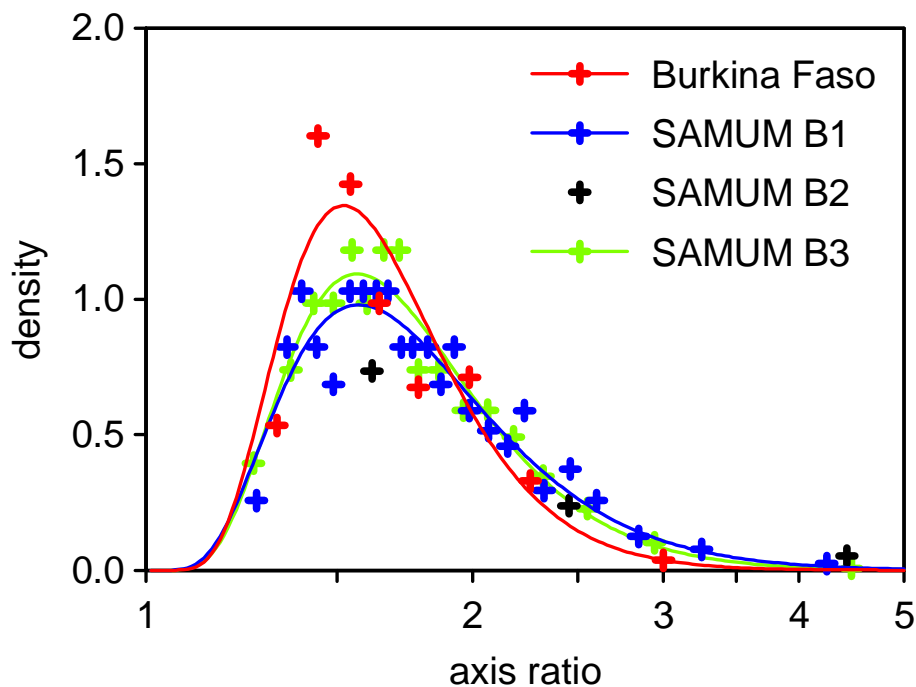


Fig. 6. Ellipse axis ratio density distributions for the soil-generated aerosol samples. The solid lines are modified log-normal functions fitted to the data. For the function description refer to Kandler et al. (2007). SAMUM B2 did not yield enough particle counts for a parameterisation.

[Title Page](#)[Abstract](#)[Introduction](#)[Conclusions](#)[References](#)[Tables](#)[Figures](#)[◀](#)[▶](#)[◀](#)[▶](#)[Back](#)[Close](#)[Full Screen / Esc](#)[Printer-friendly Version](#)[Interactive Discussion](#)

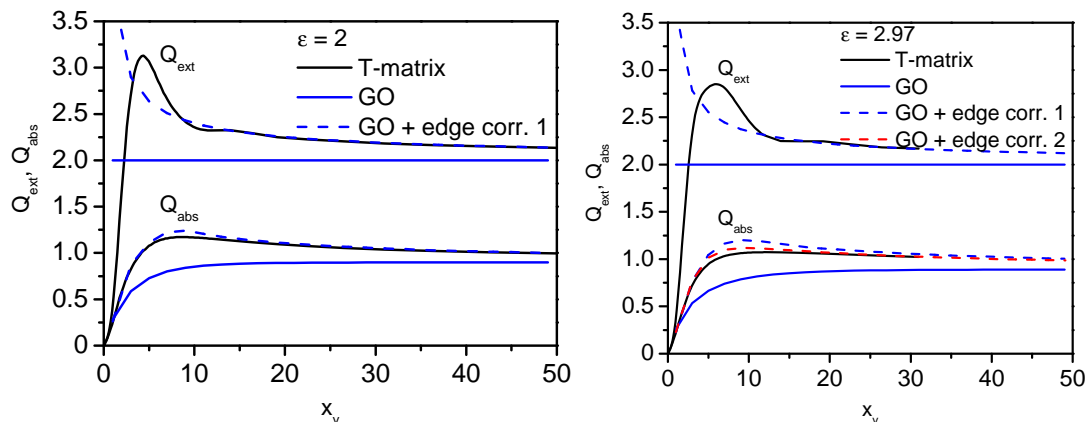


Fig. 7. Computed extinction, Q_{ext} , and absorption, Q_{abs} , efficiencies for randomly oriented oblate spheroids with an aspect ratio, ϵ , of 2 (left panel) and 2.97 (right panel) as a function of the (equal-volume sphere) size parameter x_v . The employed complex refractive index was $1.5 + 0.1i$. The black lines denote calculations with the T-matrix method and the blue lines computations with the ray tracing method including diffraction (GO: geometric optics). The dashed blue lines represent corrected geometric optics results including an edge correction that was calculated for Q_{ext} from the equations by Fournier and Evans (1991) and that was for Q_{abs} equated to the edge contribution of an equal-volume sphere. The dashed red line in the right panel denotes an improved edge correction to Q_{abs} for the $\epsilon = 2.97$ spheroid which was calculated from the edge contribution of an equal-volume spheroid of $\epsilon = 2$. See text for details.

Complex refractive indices of Saharan dust samples

R. Wagner et al.

Title Page

Abstract

Introduction

Conclusions

References

Tables

Figures

◀

▶

◀

▶

Back

Close

Full Screen / Esc

Printer-friendly Version

Interactive Discussion



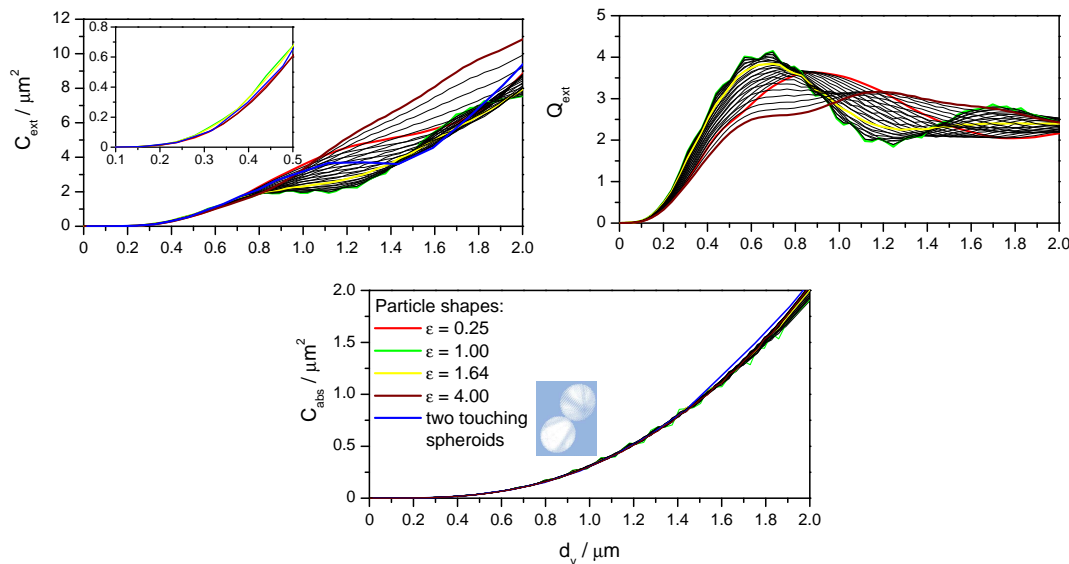


Fig. 8. Shape dependency of the optical cross sections and efficiencies of randomly oriented spheroidal particles. Left panel: extinction cross sections for all 29 considered particle shapes between $\varepsilon = 0.25$ and $\varepsilon = 4.0$. Results of selected shapes are highlighted by coloured curves, as denoted in the legend of the bottom panel. In addition to the solitary spheroids, also the extinction cross sections of an aggregate particle composed of two touching spheroids (aggregate in random orientation) are shown (blue curve). The results are extracted from our database (see Sect. 4.1) for a wavelength of 500 nm and a complex refractive index of $1.5 + 0.014 i$. The insert shows the results for the coloured curves in an expanded view covering equal-volume sphere diameters from 0.1 to 0.5 μm . Right panel: same set of calculations as in the left panel, now expressed as extinction efficiency. Bottom panel: absorption cross sections for all 29 considered spheroidal particle shapes between $\varepsilon = 0.25$ and $\varepsilon = 4.0$ as well as the aggregate particle for a complex refractive index of $1.5 + 0.014 i$ and a wavelength of 500 nm. See text for details.

Complex refractive indices of Saharan dust samples

R. Wagner et al.

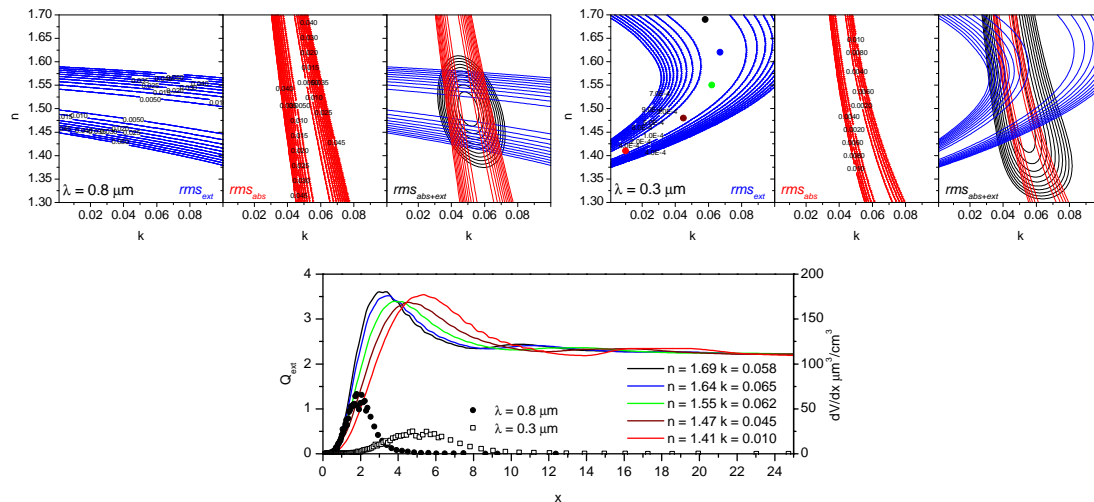


Fig. 9. Top row: contour plots of the root mean square deviations rms_{ext} (blue lines), rms_{abs} (red lines), and $rms_{abs+ext}$ (black lines) in the n and k space, as computed according to Eq. (4) in relation to the extinction and absorption coefficients for $n = 1.5$ and $k = 0.05$ at $\lambda = 0.8 \mu\text{m}$ (left part) and $\lambda = 0.3 \mu\text{m}$ (right part). The calculations were done for randomly oriented spheroids with $\varepsilon = 2$ using the measured number size distribution from Exp. 1 as input. See text for a detailed description. For the sake of clarity, only contour lines in the vicinity of the minima of the various rms values are shown. For the same reason, the contour lines for $rms_{abs+ext}$ are not labelled. The coloured points in the rms_{ext} chart of the $\lambda = 0.3 \mu\text{m}$ computation denote a series of selected complex refractive indices for which the extinction efficiencies, Q_{ext} , of the spheroids as a function of their size parameter, x , are shown with the same colour code in the bottom panel. This chart also contains the size distribution from Exp. 1 that was employed in the calculations, having been transformed into a volume size distribution on the size parameter scale, dV/dx , for $\lambda = 0.8 \mu\text{m}$ (circles) and $\lambda = 0.3 \mu\text{m}$ (squares).

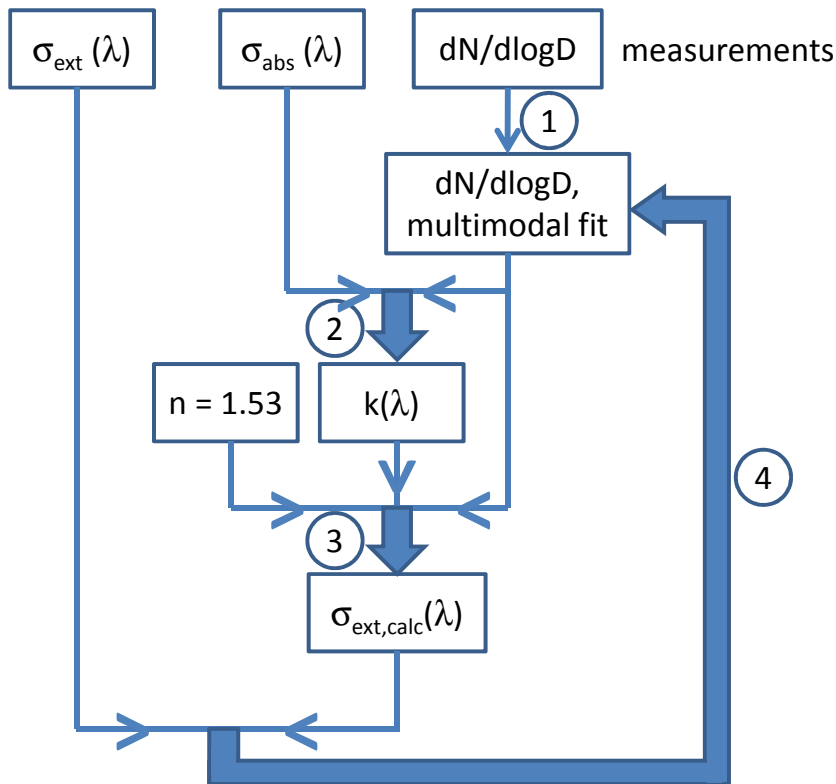


Fig. 10. Flowchart of the modified retrieval approach to deduce the wavelength dependent spectrum of the imaginary part of the complex refractive index, $k(\lambda)$, from the optical measurements. The concept involves the optimisation of the measured number size distribution of the dust particles. The individual retrieval steps 1–4 are explained in the text.

Complex refractive indices of Saharan dust samples

R. Wagner et al.

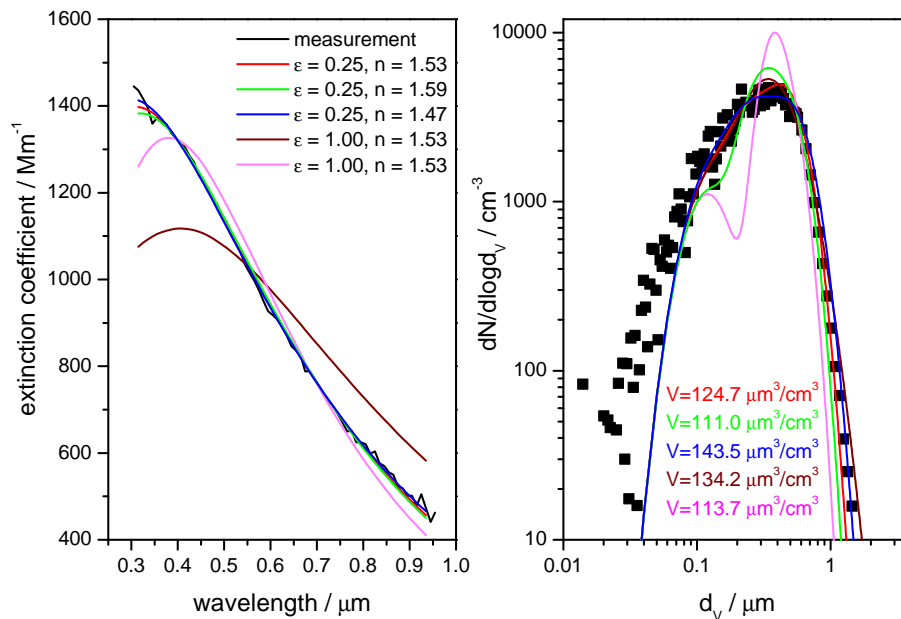


Fig. 11. Measured extinction spectrum (left panel, black line) and number size distribution (right panel, black squares) of re-dispersed dust particles from the SAMUM B3 soil sample (Exp. 8). The recordings are compared to best fit results for different assumptions on the particle shape and the real part of the complex refractive index (coloured lines), see text for details. The total volume concentrations, V , of the dust particle loading, as calculated from the various fitted number size distributions, are indicated in the right panel.

[Title Page](#)
[Abstract](#)
[Introduction](#)
[Conclusions](#)
[References](#)
[Tables](#)
[Figures](#)
[◀](#)
[▶](#)
[◀](#)
[▶](#)
[Back](#)
[Close](#)
[Full Screen / Esc](#)
[Printer-friendly Version](#)
[Interactive Discussion](#)


Complex refractive indices of Saharan dust samples

R. Wagner et al.

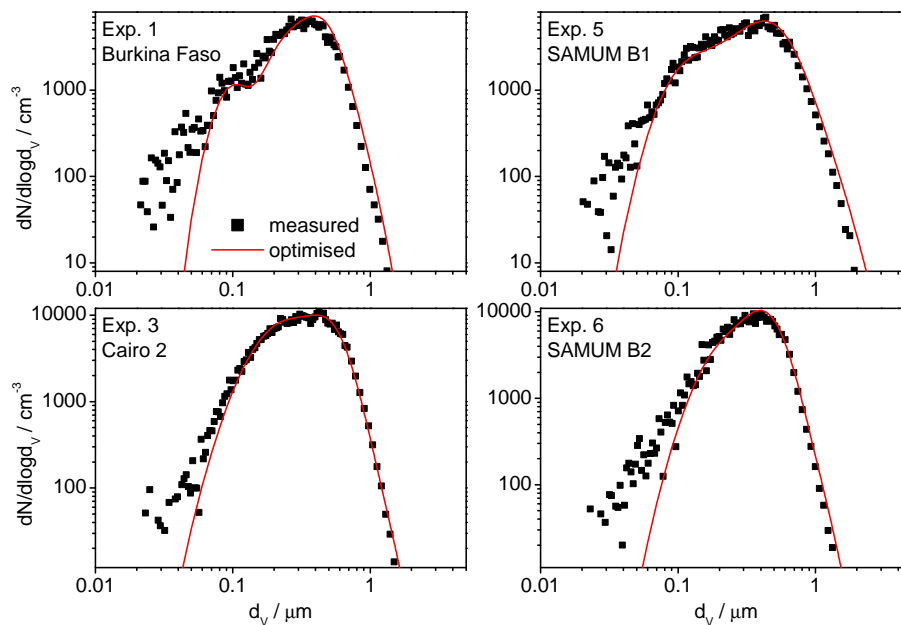


Fig. 12. Comparison between measured (black squares) and optimised (red lines) number size distributions for four further experiments with the re-dispersed Saharan dust samples.

Title Page

Abstract

Introduction

Conclusions

References

Tables

Figures

◀

▶

◀

▶

Back

Close

Full Screen / Esc

Printer-friendly Version

Interactive Discussion



Complex refractive indices of Saharan dust samples

R. Wagner et al.

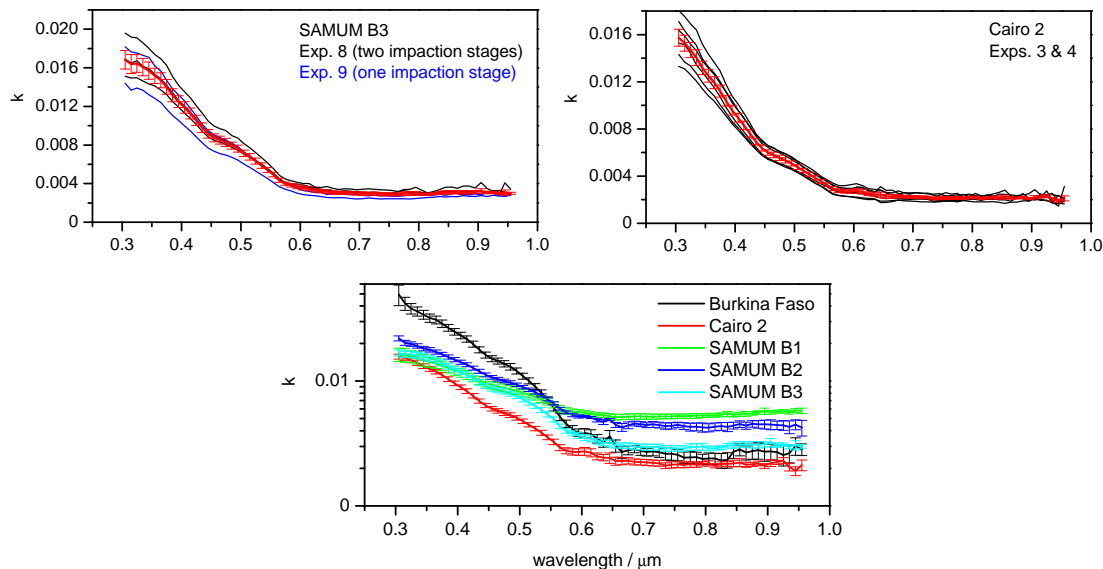


Fig. 13. Left panel: retrieved spectra of the imaginary part of the complex refractive index, k , for the SAMUM B3 dust sample from individual measurements during Exp. 8 (black lines) and Exp. 9 (blue lines). The resulting mean k spectrum and its standard error, denoting the variability between the individual measurement cycles, are shown in red. Right panel: retrieved k spectra for the Cairo 2 dust sample from six individual measurements during Exps. 3 and 4 (black lines). As in the left panel, the mean k spectrum and its standard error are shown in red. Bottom panel: mean k spectra and their standard error for all five investigated dust samples on a logarithmic k scale.

[Title Page](#)
[Abstract](#)
[Introduction](#)
[Conclusions](#)
[References](#)
[Tables](#)
[Figures](#)
[◀](#)
[▶](#)
[◀](#)
[▶](#)
[Back](#)
[Close](#)
[Full Screen / Esc](#)
[Printer-friendly Version](#)
[Interactive Discussion](#)


Complex refractive indices of Saharan dust samples

R. Wagner et al.

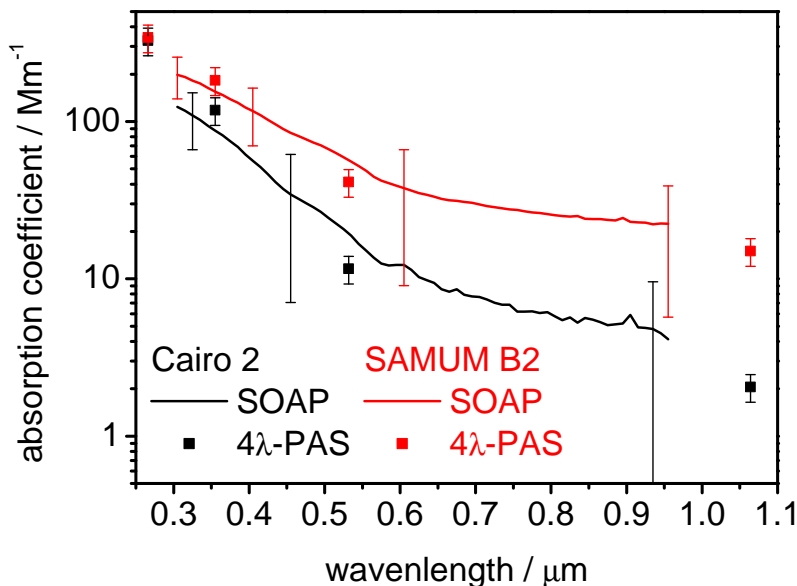


Fig. 14. Comparison of the absorption coefficients measured by SOAP and 4λ – PAS for re-dispersed dust particles from the Cairo 2 and SAMUM B2 soil samples. Maximum uncertainties of SOAP were computed according to $\Delta\sigma_{\text{abs}} = \pm (0.15 \sigma_{\text{abs}} + 0.02 \sigma_{\text{sca}})$, see Sect. 2.2. For the 4λ – PAS, an uncertainty of $\pm 20\%$ was assumed. This reflects maximum deviations from reference instruments which were observed in recent test measurements (Ajtai et al., 2010). Further inter-comparison measurements are needed to better assess the uncertainty of both techniques.

[Title Page](#)
[Abstract](#)
[Introduction](#)
[Conclusions](#)
[References](#)
[Tables](#)
[Figures](#)
[◀](#)
[▶](#)
[◀](#)
[▶](#)
[Back](#)
[Close](#)
[Full Screen / Esc](#)
[Printer-friendly Version](#)
[Interactive Discussion](#)


Complex refractive indices of Saharan dust samples

R. Wagner et al.

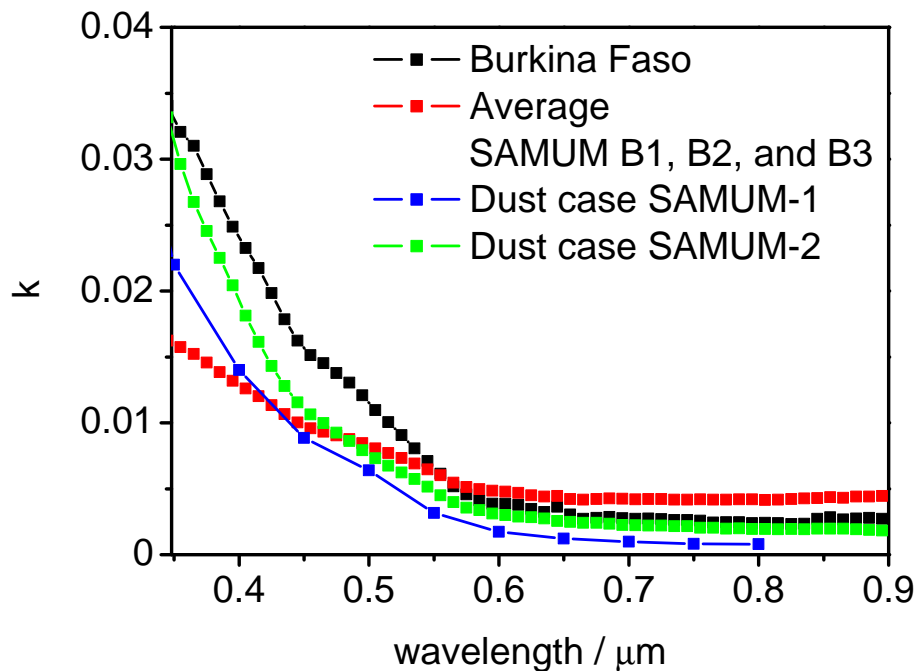


Fig. 15. Retrieved k spectrum for the Burkina Faso dust probe and averaged k spectrum for the three SAMUM B1, B2, and B3 dust samples from this study in comparison with imaginary parts of refractive indices derived during the SAMUM-1 and SAMUM-2 field campaigns for typical dust cases; see Fig. 8 in Müller et al. (2011).

[Title Page](#)[Abstract](#)[Introduction](#)[Conclusions](#)[References](#)[Tables](#)[Figures](#)[◀](#)[▶](#)[◀](#)[▶](#)[Back](#)[Close](#)[Full Screen / Esc](#)[Printer-friendly Version](#)[Interactive Discussion](#)

Complex refractive indices of Saharan dust samples

R. Wagner et al.

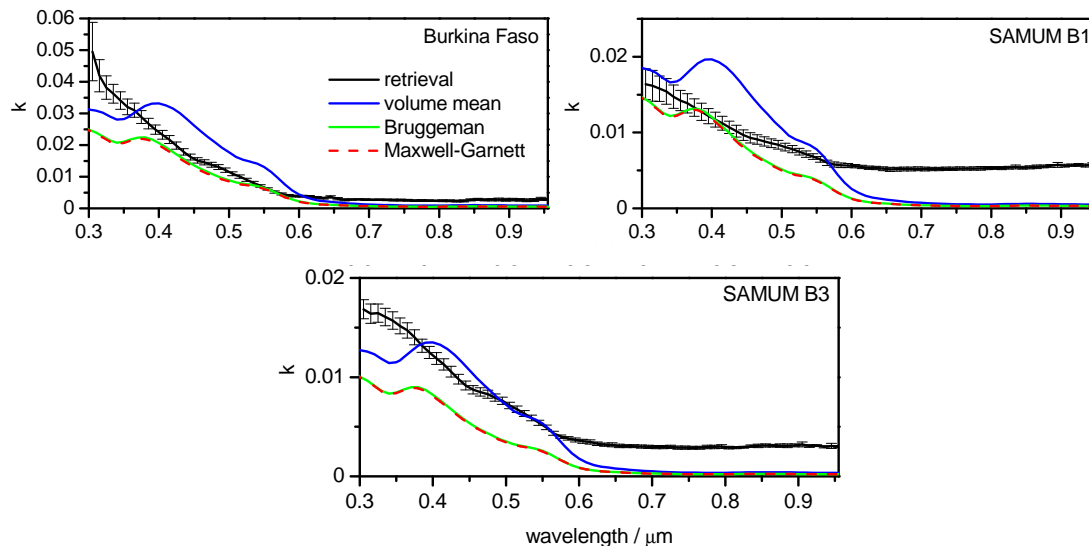


Fig. 16. Comparison of the retrieved k spectra for the re-dispersed Burkina Faso, SAMUM B1, and SAMUM B3 soil samples with those computed with various mixing rule approaches (volume mean, Bruggeman, and Maxwell-Garnett approximation; see Sokolik and Toon, 1999), employing the hematite volume abundances derived from the single particle analyses of the mineralogical composition (Table 4). See text for details.

Title Page

Abstract

Introduction

Conclusions

References

Tables

Figures

◀

▶

◀

▶

Back

Close

Full Screen / Esc

Printer-friendly Version

Interactive Discussion

